INTERNATIONAL JOURNAL FOR NUMERICAL METHODS IN ENGINEERING
Int. J. Numer. Meth. Engng 2000; **00**:1–6 *Prepared using* nmeauth.cls *[Version: 2002/09/18 v2.02]*

Discontinuous Galerkin Methods for Nonlinear Elasticity

Ten Eyck A., Lew A.*

Department of Mechanical Engineering, Stanford University, CA 94305-4040

SUMMARY

This paper presents the formulation and a partial analysis of a class of discontinuous Galerkin methods for quasistatic nonlinear elasticity problems. These methods are endowed with several salient features. The equations that define the numerical scheme are the Euler–Lagrange equations of a one–field variational principle, a trait that provides an elegant and simple derivation of the method. In consonance with general discontinuous Galerkin formulations, it is possible within this framework to choose different numerical fluxes. Numerical evidence suggests the absence of locking at near incompressible conditions in the finite deformations regime when piecewise linear elements are adopted. Finally, a conceivable surprising characteristic is that, as demonstrated with numerical examples, these methods provide a given accuracy level for a comparable, and often lower, computational cost than conforming formulations.

Stabilization is occasionally needed for discontinuous Galerkin methods in linear elliptic problems. In this paper we propose a sufficient condition for the stability of each linearized nonlinear elastic problem that naturally includes material and geometric parameters; the latter needed to account for buckling. We then prove that when a similar condition is satisfied by the discrete problem, the method provides stable linearized deformed configurations upon the addition of a standard stabilization term.

We conclude by discussing the complexity of the implementation, and propose a computationally efficient approach that avoids looping over both elements and element faces. Several numerical examples are then presented in two and three dimensions that illustrate the performance of a selected discontinuous Galerkin method within the class.

KEY WORDS: Nonlinear elasticity, discontinuous Galerkin, stabilization, incompressibility, locking

Contents

*Correspondence to: Department of Mechanical Engineering, Stanford University, CA 94305-4040. Email:lewa@stanford.edu

Contract/grant sponsor: National Institutes of Health, NIH Roadmap for Medical Research; contract/grant number: U54 GM072970

Received
Revised

1. INTRODUCTION

This paper presents the formulation and a partial analysis of a class of discontinuous Galerkin (DG) methods for quasistatic nonlinear elasticity problems. These methods are endowed with several salient features. The equations that define the numerical scheme are the Euler–Lagrange equations of a one–field variational principle, a trait that provides an elegant and simple derivation of the methods and brings their computational complexity and cost in line with the most efficient existing ones. In consonance with general discontinuous Galerkin formulations, it is possible within this framework to choose different numerical fluxes. Numerical evidence suggests the absence of locking at near incompressible conditions in the finite deformations regime when piecewise linear elements are adopted. Finally, a conceivable surprising characteristic is that, as demonstrated with numerical examples, these methods provide a given accuracy level for a comparable, and often lower, computational cost than conforming formulations, i.e., where no discontinuities across elements are permitted.

Nonlinear elasticity theory is widely utilized in modeling the mechanical behavior of soft materials, particularly in the phenomenological description of elastomers [38] and human tissue, such as muscle[6], blood vessels [17] and the cornea[28]. Martensitic transformations in metals and metal alloys, such as shape memory alloys, are also well described within the nonlinear elasticity framework [29, 11]. In all these situations, the inherent nonlinearities in the theory are crucial for their success.

The numerical solution of nonlinear elasticity problems is hindered by a number of challenges. Conspicuous among these are problems related to capturing solutions in which the material

develops a very fine microstructure, see [10] for a recent perspective. These highly oscillatory deformations are generally a direct consequence of the lack of convexity of the strain energy density of the material. In fact, more often than not exact solutions for these problems in the sense of Sobolev functions do not exist; solutions can exist, however, as Young measures. Localization of deformation plagues nonlinear elastic behavior as well, most prominently in the form of shear bands, cavitation and, if Griffith theory is adopted, brittle fracture [24]. The fact that these localized singularities may ubiquitously appear in the body imposes seemingly impossible requirements on the discretization scheme. For a fairly recent perspective on the status of nonlinear elasticity theory we refer the reader to [4], where a number of open problems are stated and discussed.

Notwithstanding these singularities, there are situations in which deformations are smooth; in these cases numerical approximations to solutions of the equilibrium equations can be obtained through more traditional methodologies, such as some type of finite element method. The class of numerical methods introduced here were designed to address precisely this type of problems. We shall speculate, however, that discontinuous Galerkin methods may prove useful for some non–smooth problems as well, as the experience with shock–capturing for hyperbolic problems dictates. For situations in which a fine microstructure is developed the nonconforming approximation is likely to allow a localized enrichment of the discrete functional space, in the spirit of [20, 18, 13].

In this paper we draw from the discontinuous Galerkin method presented in [22] for linear elasticity to formulate a class of methods for the nonlinear elastic case. The method in [22] adopts the numerical fluxes of Bassi and Rebay [5], following the work in [9] for the scalar diffusion equation. More generally, a quite comprehensive description of discontinuous Galerkin methods for elliptic problems (see, e.g., [19, 27, 26, 39, 1, 30, 16, 3, 40, 12]) can be found in [2], which provides a common framework for most proposed methods. In [22], an elementwise Hu–Washizu variational principle is used to derive the numerical method when restricted to discrete sets of displacements, strains and stresses that are possibly discontinuous across element boundaries. The method shares a number of features with others also stemming from the Hu–Washizu variational principle, e.g., [32, 34], most prominent among them are assumed strain methods, see, e.g., [35, 33, 14]. The obvious difference is that the methods we present here use discontinuous approximations for the displacements.

A major drawback of the use of three–field variational principles is that the computational cost can be overwhelming. As a result, a different perspective was adopted, in which we obtain the methods through their primal formulation. To this end, after briefly discussing the nonlinear elasticity problem in section 2, we recall the relationship between the exact and approximated derivative of a field for discontinuous Galerkin discretizations in section 3; we call the latter the DG-derivative. The numerical scheme is simply and elegantly derived through a discrete variational principle in section 3.2. It consists of finding a local minimum potential energy configuration of the body among all possible discrete configurations, with the caveat that the gradient of the deformation mapping is evaluated through the DG–derivative. It is precisely within the DG–derivative where all the information about the chosen numerical fluxes and approximation space for the derivatives can be found. In section 3.4 we show how an equivalent three–field variational principle, of the Hu–Washizu type, can be recovered from this formulation, including the method for linear elasticity in [22].

A driving force behind the development of nonconforming and mixed-methods for elasticity has been the appearance of locking in one–field conforming approximations when kinematic

constraints are imposed, such as incompressibility. When linearized kinematics are adopted, the latter takes the well known form of a divergence–free constraint on the displacement field. Solutions for this problem in the linear elasticity case are well known, such as reduced integration, mixed methods, enhanced strain methods, assumed strain methods and discontinuous Galerkin methods, among others. Some of these ideas remain valid when nonlinear constitutive equations are adopted with either linearized [14] or exact [36] kinematic descriptions. The numerical examples in section 6.6 suggest that when the Bassi and Rebay numerical fluxes are chosen, together with piecewise linear elements, the resulting discontinuous Galerkin method is locking–free for nearly incompressible situations with the body undergoing large deformations, a notable advantage over mixed methods that need to carry the extra pressure field.

It was shown in [22], closely following the developments in [9], that the choice of Bassi and Rebay numerical fluxes for the linear elastic case results in a discrete bilinear form that may not be coercive, i.e., unstable. Nonetheless, the addition of standard discontinuous Galerkin stabilization renders the discrete problem stable for any positive choice of the stabilization parameter. A similar feature should be present in the nonlinear extension, however, the exact stability requirement in this case is not at all evident. For example, as discussed in section 4, it is very restrictive to request the elastic moduli at each linearized configuration of the body to be uniformly positive semidefinite, a key assumption in the stress–free linear elastic case. In fact, some eigenvalues of the elastic moduli can be negative at all points in space, but the linearized elasticity problem still be coercive. For instance, from the discussion in section 4 it can easily be seen that the elastic moduli in a body at equilibrium under spatially uniform compressive pressure has some negative eigenvalues at every point. Notwithstanding, it is possible for the potential energy to only increase when any infinitesimal displacement field that is zero on the boundary is superimposed on the body, i.e., the configuration may be stable.

In section 4 we propose a more general sufficient condition on the elastic moduli at each linearized configuration that, if satisfied, leads to the coercivity of the linearized elasticity problem. In it, information from both the constitutive relation and the geometry of the deformed body is involved. Given that buckling is often geometric in nature, the inclusion of a geometric factor comes with no surprise. The key contribution in this section is Theorem 4.1, which, at a deformed configuration, compares the coercivity of the bilinear form associated with the exact linearized elasticity problem with that of the second variation of the stabilized discontinuous Galerkin method. The proof of the theorem relies heavily in a generalized version of Korn's inequality [25]; its constant provides the geometric information in the stability condition. We prove that, under certain conditions, the bilinear form in the second variation of the stabilized method is coercive provided the stabilization parameter is large enough, a somewhat striking difference with the results of the standard stress–free linear elasticity problem. We cannot yet guarantee, however, that this bilinear form is coercive whenever the exact one is. The consequences of this theorem are consistent with the behavior of the numerical examples shown in section 6.3.

The numerical examples in section 6.4 show the somehow unexpected result that the computational cost of computing a solution at a given accuracy is often *equal* or *cheaper* with a discontinuous Galerkin approach than with a conforming method. Alternatively, this means that discontinuous Galerkin methods often furnish equally accurate solutions with coarser meshes. In contrast with established misconceptions, this shows that discontinuous Galerkin

methods in a primal formulation *are* computationally efficient. Of course, when a very large value for the stabilization parameter is adopted, this advantage is lost, since the discontinuous Galerkin scheme behaves as the conforming approximation. Likewise, as finer meshes are used, the size of the jumps in the numerical solution wanes, giving up any advantage of discontinuous Galerkin methods; see section 6.4.

Finally, in section 6.2 we show a numerical example in which a conforming approximation fails to respect the symmetries of a problem, regardless of how much the mesh is recursively refined. This is a direct consequence of the particular sequence of meshes chosen to solve it. On *exactly* the same meshes, a discontinuous Galerkin method performs ostensibly better; it takes advantage of the possible discontinuities across elements to relax the rigid kinematic constraints imposed by the mesh. Section 6.7 presents selected three–dimensional numerical examples that establish the feasibility of utilizing this approach for realistic complex configurations.

Throughout the paper v_i, φ_i, ..., denote components of vectors and w_{ij}, F_{iJ}, ..., components of second–order tensors, with respect to a Cartesian basis in $\mathbb{R}^d$. As conventionally done, uppercase letters are used for tensor components in the reference configuration, while lowercase letters are reserved for spatial indices. We also adopt the summation convention in which repeated indices indicate sum, its range tacitly determined from the context.

2. NONLINEAR ELASTICITY PROBLEM

We consider a body with reference configuration $\mathcal{B}_0 \in \mathbb{R}^d$ that deforms under the action of external loads. For simplicity we assume that $\mathcal{B}_0$ is a polyhedron with a connected interior. Because of the deformation, a point $\mathbf{X} \in \mathcal{B}_0$ is mapped to a point $\mathbf{x} = \boldsymbol{\varphi}(\mathbf{X})$ in the deformed configuration, where $\boldsymbol{\varphi}\colon \mathcal{B}_0 \mapsto \mathbb{R}^d$ is the deformation mapping. We are concerned here with simple nonlinear elastic bodies; i.e., made out of materials for which there exists a strain energy density function $W : \mathcal{B}_0 \times \mathbb{R}^{d\times d} \mapsto \mathbb{R}$, $W(\mathbf{X}, \mathbf{F})$, where $\mathbf{F} = \nabla\boldsymbol{\varphi}(\mathbf{X})$ is commonly known as the deformation gradient at point $\mathbf{X}$. For these materials, the first Piola–Kirchhoff stress tensor follows as $\mathbf{P} = \partial W/\partial\mathbf{F}$. In addition, the strain energy density function is assumed to satisfy the postulate of material frame indifference [23]. Therefore, there exists a function $\hat{W}(\mathbf{X}, \mathbf{C})$, with $\mathbf{C}$ symmetric, such that $W(\mathbf{X}, \mathbf{F}) = \hat{W}(\mathbf{X}, \mathbf{F}^{\mathsf{T}}\mathbf{F})$; the strain energy density is invariant under superimposed rigid body rotations.

Static equilibrium configurations of the body are given by the stationary points of the potential energy functional

$$I[\boldsymbol{\varphi}] = \int_{\mathcal{B}_0} W(\mathbf{X}, \nabla\boldsymbol{\varphi})\ dV - \int_{\partial_\tau\mathcal{B}_0} \overline{\mathbf{T}} \cdot \boldsymbol{\varphi}\ dS. \tag{1}$$

More precisely, we seek deformation mappings $\boldsymbol{\varphi} \in V$ such that

$$\langle \delta I[\boldsymbol{\varphi}], \delta\boldsymbol{\varphi}\rangle = \left.\frac{\partial}{\partial\varepsilon} I[\boldsymbol{\varphi}^\varepsilon]\right|_{\varepsilon=0} = 0, \tag{2}$$

for all admissible variations $\delta\boldsymbol{\varphi} = \partial\boldsymbol{\varphi}^\varepsilon/\partial\varepsilon|_{\varepsilon=0}$, where $\boldsymbol{\varphi}^\varepsilon \in V$ is a smooth one–parameter family of deformation mappings in V such that $\boldsymbol{\varphi} = \boldsymbol{\varphi}|_{\varepsilon=0}$ (see, e.g., [23]). External tractions $\overline{T}(\mathbf{X})$ are applied on $\partial_\tau\mathcal{B}_0 \subseteq \partial\mathcal{B}_0$, while any $\boldsymbol{\varphi}$ in the set of admissible deformation mappings V is required to have prescribed values $\overline{\boldsymbol{\varphi}}(\mathbf{X})$ on $\partial_d\mathcal{B}_0 \subseteq \partial\mathcal{B}_0$. For simplicity, we assume that

$\partial_\tau \mathcal{B}_0 \cap \partial_d \mathcal{B}_0 = \emptyset$, $\partial_\tau \mathcal{B}_0 \cup \partial_d \mathcal{B}_0 = \partial \mathcal{B}_0$ and that $\partial_d \mathcal{B}_0$ has positive $\mathcal{H}^{d-1}$–measure[†], to prevent rigid body motions. Body forces can also be accounted for in a straightforward way.

Only local minimizers of the potential energy functional (1) are stable under small perturbations, and hence often the solutions of interest. Herein we assume that conditions for minimizers to exist, such as W being polyconvex (see, e.g., [4]), are met.

For future reference, it is convenient to introduce two other stress tensors, i.e., the second Piola–Kirchhoff stress tensor $\mathbf{S} = 2\partial \hat{W}/\partial \mathbf{C} = \mathbf{F}^{-1}\mathbf{P}$ and the Kirchhoff stress tensor $\boldsymbol{\tau} = \mathbf{P}\mathbf{F}^{\mathsf{T}}$. In Cartesian components, $S_{IJ} = F^{-1}_{Ii} P_{iJ}$ and $\tau_{ij} = P_{iJ} F_{jJ}$. While $\mathbf{P}$ is not necessarily symmetric, both $\mathbf{S}$ and $\boldsymbol{\tau}$ are. For completeness, the Cauchy stress tensor is obtained as $\boldsymbol{\sigma} = (\det \mathbf{F})^{-1} \boldsymbol{\tau}$. Associated with these stress tensors, we introduce the first and second elasticity tensors, $\mathbb{A} = \partial^2 W/\partial \mathbf{F}^2$ and $\mathbb{C} = 2\partial^2 \hat{W}/\partial \mathbf{C}^2$, respectively. The relation between these two tensors is given by, in Cartesian components,

$$\mathbb{A}_{iJkL}(\mathbf{X}, \mathbf{F}) = 2\mathbb{C}_{IJKL}(\mathbf{X}, \mathbf{F}^{\mathsf{T}}\mathbf{F}) F_{iI} F_{kK} + S_{JL}(\mathbf{X}, \mathbf{F}^{\mathsf{T}}\mathbf{F}) \delta_{ik}, \tag{3}$$

where δ_{ik} denotes the Kronecker delta. It follows from the definition that $\mathbb{A}$ has only major symmetries, $\mathbb{A}_{iJkL} = \mathbb{A}_{kLiJ}$, while $\mathbb{C}$ has both major and minor symmetries, $\mathbb{C}_{IJKL} = \mathbb{C}_{KLIJ} = \mathbb{C}_{JIKL}$. For more details about the relation between these nonlinear elasticity concepts we refer the reader to [23].

3. DISCONTINUOUS GALERKIN DISCRETIZATION

In the following, we briefly outline basic definitions needed in formulating discontinuous Galerkin methods; we refer the readers to [22, 2] for more comprehensive statements.

Let $\mathcal{T}_h$ be a conforming finite element mesh on $\mathcal{B}_0$. Each element $E \in \mathcal{T}_h$ is assumed to be an open polyhedron with an orientable boundary ∂E and unit outward normal $\mathbf{N}^E$. Let e denote an arbitrary element face, and $\Gamma = \cup_{E \in \mathcal{T}_h} \partial E$ be the set of all element faces. We assume that the latter can be decomposed into three subsets, namely

$$\Gamma^I = \{e \subset \partial E \setminus \partial \mathcal{B}_0 : E \in \mathcal{T}_h\} \tag{4}$$

$$\Gamma^d = \{e \subset \partial E \cap \partial_d \mathcal{B}_0 : E \in \mathcal{T}_h\} \tag{5}$$

$$\Gamma^\tau = \{e \subset \partial E \cap \partial_\tau \mathcal{B}_0 : E \in \mathcal{T}_h\}, \tag{6}$$

such that $\Gamma = \Gamma^I \cup \Gamma^d \cup \Gamma^\tau$. We assign an orientation to each face $e \in \Gamma^I$. Henceforth we will denote E^+ and E^- the two elements that satisfy $E^+ \cap E^- = e$, with $\mathbf{N}$ being the outward normal to E^-. For faces $e \in \Gamma \setminus \Gamma^I$, $\mathbf{N}$ simply denotes the outward normal to $\mathcal{B}_0$.

Let V_h^E be a discrete vector space of smooth scalar (e.g., C^∞) functions in an element E. For example, V_h^E can be the set of linear polynomials in a tetrahedral element. A discontinuous Galerkin finite element space is constructed as $V_h = \Pi_{E \in \mathcal{T}_h} V_h^E$, which allows functions in V_h to be discontinuous across element faces in Γ^I. We shall consider two types of such spaces, V_h and W_h, with $V_h \subseteq W_h$; and shall use V_h^d and $W_h^{d \times d}$ to approximate the deformation mapping and its gradient, respectively. For definiteness, we choose to approximate each Cartesian component of a vector or, more generally, a tensor with functions in V_h or W_h. Herein, we shall additionally

[†]Hausdorff measure

assume that $\nabla V_h \subseteq W_h^d$, to be used in defining the discontinuous Galerkin derivative in section 3.1. It is also useful to define $T(\Gamma) = \Pi_{E\in\mathcal{T}_h} L^2(\partial E)$, which contains bi–valued functions on Γ^I and single–valued on $\Gamma \setminus \Gamma^I$.

3.1. Derivatives within Discontinuous Galerkin

Next, we would like to define a *discrete discontinuous Galerkin derivative* operator; we do so by following the derivation of discontinuous Galerkin primal formulations (see [2]). We shall use this derivative operator to formulate a variety of discontinuous Galerkin methods for nonlinear elasticity.

As detailed in [2], the starting point for the formulation of discontinuous Galerkin methods is the identity

$$\int_E \mathbf{w}\cdot\mathbf{z}\; dV = \int_{\partial E} \hat{v}\otimes\mathbf{N}^E\cdot\mathbf{z}\; dS - \int_E v\nabla\cdot\mathbf{z}\; dV, \tag{7}$$

which holds for any element $E \in \mathcal{T}_h$ and for all $\mathbf{z} \in W_h^d$. In equation (7), $v \in V_h$, and $\mathbf{w} \in W_h^d$ is an approximation to its derivative which we would like to solve for. The use of the tensor product in equation (7) guarantees that the same expression holds when replacing v for a vector field, such as the deformation mapping. The design of the discontinuous Galerkin method is embedded in the choice of the so–called numerical flux $\hat{v}$, that takes a function in V_h and returns a numerical approximation to its values on Γ, i.e., a function in $T(\Gamma)$, and therefore possibly bi–valued on Γ^I. We will only consider numerical fluxes that are linear, as most commonly done in the literature.

For convenience, we introduce the jump $[\![\cdot]\!]$ and average $\{\cdot\}$ operators for functions $v \in V_h$ and $\mathbf{z} \in W_h^d$, following the convention in [22][‡]. If $e \subset \Gamma^I$,

$$[\![v]\!] = v^- - v^+, \qquad \{v\} = \frac{1}{2}\left(v^+ + v^-\right) \tag{8}$$

$$[\![\mathbf{z}]\!] = \mathbf{z}^- - \mathbf{z}^+, \qquad \{\mathbf{z}\} = \frac{1}{2}\left(\mathbf{z}^+ + \mathbf{z}^-\right), \tag{9}$$

where the $+$ and $-$ superscripts correspond to evaluating the functions at either side of e, i.e., at the elements E^+ and E^- such that $e = \overline{E^+} \cap \overline{E^-}$. If $e \in \Gamma \setminus \Gamma^I$ we only need to define

$$[\![v]\!] = v, \qquad \{\mathbf{z}\} = \mathbf{z}, \tag{10}$$

Note that while the definition of the jump depends on the chosen orientation for e, the quantity $[\![\cdot]\!]\otimes\mathbf{N}$ does not.

It then follows from equation (7) that

$$\sum_{E\in\mathcal{T}_h}\int_E \mathbf{w}\cdot\mathbf{z}\; dV = \sum_{E\in\mathcal{T}_h}\int_{\partial E} \hat{v}\otimes\mathbf{N}^E\cdot\mathbf{z}\; dS - \sum_{E\in\mathcal{T}_h}\int_E v\nabla\cdot\mathbf{z}\; dV \tag{11}$$

$$= \int_\Gamma [\![\hat{v}]\!]\otimes\mathbf{N}\cdot\{\mathbf{z}\}\; dS + \int_{\Gamma^I}\{\hat{v}\}\otimes\mathbf{N}\cdot[\![\mathbf{z}]\!]\; dS - \sum_{E\in\mathcal{T}_h}\int_E v\nabla\cdot\mathbf{z}\; dV, \tag{12}$$

[‡]These definitions are not uniform across the literature. See, e.g. [2] or [9] for examples of other conventions.

which can be obtained by a straightforward rearrangement of the terms. Comparing this expression with the integration by parts formula for smooth functions v and $\mathbf{z}$ with possible discontinuities on Γ

$$\sum_{E\in\mathcal{T}_h}\int_E \nabla v\cdot\mathbf{z}\;dV=\int_\Gamma [\![v]\!]\otimes\mathbf{N}\cdot\{\mathbf{z}\}\;dS+\int_{\Gamma^I}\{v\}\otimes\mathbf{N}\cdot[\![\mathbf{z}]\!]\;dS-\sum_{E\in\mathcal{T}_h}\int_E v\nabla\cdot\mathbf{z}\;dV, \quad (13)$$

we obtain

$$\sum_{E\in\mathcal{T}_h}\int_E(\mathbf{w}-\nabla v)\cdot\mathbf{z}\;dV=\int_\Gamma [\![\hat{v}-v]\!]\otimes\mathbf{N}\cdot\{\mathbf{z}\}\;dS+\int_{\Gamma^I}\{\hat{v}-v\}\otimes\mathbf{N}\cdot[\![\mathbf{z}]\!]\;dS. \quad (14)$$

Equation (14) holds for all $\mathbf{z}\in W_h^d$, and uniquely defines the discontinuous Galerkin derivative $\mathbf{w}$. This equation can be explicitly solved for $\mathbf{w}$ by introducing the *lifting operators* $\mathbf{R}:L^2(\Gamma)\mapsto W_h^d$ and $\mathbf{L}:L^2(\Gamma^I)\mapsto W_h^d$, defined to satisfy[§]

$$\int_{\mathcal{B}_0}\mathbf{R}(v)\cdot\mathbf{z}\;dV=-\int_\Gamma v\otimes\mathbf{N}\cdot\{\mathbf{z}\}\;dS,\qquad \int_{\mathcal{B}_0}\mathbf{L}(v)\cdot\mathbf{z}\;dV=-\int_{\Gamma^I}v\otimes\mathbf{N}\cdot[\![\mathbf{z}]\!]\;dS, \quad (15)$$

for all $\mathbf{z}\in W_h^d$. A simple interpretation of the lifting operators follows after noticing that both terms on the right–hand side of equation (14) are linear operators over W_h^d, for each different v. Hence, $\mathbf{R}(v)\in W_h^d$ and $\mathbf{L}(v)\in W_h^d$ are the representatives of these linear operators obtained from the Riesz representation theorem under the L^2 scalar product in W_h^d.

Substituting in equation (14) we get

$$\sum_{E\in\mathcal{T}_h}\int_E(\mathbf{w}-\nabla v-\mathbf{R}([\![v-\hat{v}]\!])-\mathbf{L}(\{v-\hat{v}\}))\cdot\mathbf{z}\;dV=0, \quad (16)$$

for all $\mathbf{z}\in W_h^d$. Since we assumed that $\nabla V_h\subseteq W_h^d$, it follows that

$$\mathbf{w}=D_{\mathrm{DG}}v=\nabla v+\mathbf{R}([\![v-\hat{v}]\!])+\mathbf{L}(\{v-\hat{v}\}). \quad (17)$$

Equation (17) defines the operator $D_{\mathrm{DG}}:V_h\mapsto W_h^d$, which furnishes a discrete discontinuous Galerkin derivative amenable to be used in the formulation of the methods in the next section.

The operator D_{DG} has only been defined for scalar functions; however, it is trivially extended to vector fields in V_h^d, given that each Cartesian component lives in V_h. For definiteness, for $\mathbf{v}\in V_h^d$ we have $D_{\mathrm{DG}}\mathbf{v}=\mathbf{e}_i\otimes(D_{\mathrm{DG}}v_i)$, where $\mathbf{e}_i$ is a Cartesian basis in $\mathbb{R}^d$. This definition induces trivial extensions of the lifting operators such that equation (17) formally holds for vector fields. In this case, $\mathbf{R}:\left[L^2(\Gamma)\right]^d\mapsto W_h^{d\times d}$ and $\mathbf{L}:\left[L^2(\Gamma)\right]^d\mapsto W_h^{d\times d}$ are such that $\mathbf{R}(\mathbf{v})=\mathbf{e}_i\otimes\mathbf{R}(v_i)$ and $\mathbf{L}(\mathbf{v})=\mathbf{e}_i\otimes\mathbf{L}(v_i)$, for all $\mathbf{v}\in V_h^d$. Finally, the numerical flux $\hat{v}$ is also trivially extended to give $\hat{v}(\mathbf{v})=\mathbf{e}_i\hat{v}(v_i)$, for any $\mathbf{v}\in V_h^d$. We have purposely abused notation and utilized the same name for the original operators and their corresponding extensions. Henceforth, we shall leave their exact nature to be tacitly understood from the context.

[§]Once more, these definitions are not uniform across the literature, see, e.g., [22, 9].

3.2. Discrete Variational Principle

The discontinuous Galerkin method ensues by resorting to a discrete variational principle. Let $I_h : V_h^d \mapsto \mathbb{R}$ be the functional

$$I_h[\mathbf{v}] = \sum_{E\in\mathcal{T}_h} \int_E W(\mathbf{X}, D_{\mathrm{DG}}\mathbf{v})\ dV - \int_{\partial_\tau \mathcal{B}_0} \overline{\mathbf{T}} \cdot \boldsymbol{v}\ dS. \tag{18}$$

The discrete problem consists on seeking a discrete deformation mapping $\boldsymbol{\varphi} \in V_h^d$ that is a stationary point of I_h in V_h^d. The discrete Euler–Lagrange equations follow from

$$0 = \langle \delta I_h[\boldsymbol{\varphi}], \delta\boldsymbol{\varphi}\rangle = \sum_{E\in\mathcal{T}_h} \int_E \frac{\partial W}{\partial \mathbf{F}}(\mathbf{X}, D_{\mathrm{DG}}\boldsymbol{\varphi})\colon D_{\mathrm{DG}}\delta\boldsymbol{\varphi}\ dV - \int_{\partial_\tau \mathcal{B}_0} \overline{\mathbf{T}} \cdot \delta\boldsymbol{\varphi}\ dS, \tag{19}$$

for any admissible variation $\delta\boldsymbol{\varphi} = \partial\boldsymbol{\varphi}^\varepsilon/\partial\varepsilon|_{\varepsilon=0}$, where $\boldsymbol{\varphi}^\varepsilon$ is a smooth one–parameter family of discrete deformation mappings in V_h^d, such that $\boldsymbol{\varphi}^\varepsilon|_{\varepsilon=0} = \boldsymbol{\varphi}$.

Equation (19) is a nonlinear equation to be solved for $\boldsymbol{\varphi}$. If using a Newton–like iterative method, it is necessary to consider its linearization around a deformation mapping $\boldsymbol{\varphi}$, given by

$$0 = \langle \delta^2 I_h[\boldsymbol{\varphi}], \delta\boldsymbol{\varphi}, \mathbf{u}\rangle + \langle \delta I_h[\boldsymbol{\varphi}], \delta\boldsymbol{\varphi}\rangle \tag{20}$$

for all admissible $\delta\boldsymbol{\varphi}$, where

$$\langle \delta^2 I_h[\boldsymbol{\varphi}], \delta\boldsymbol{\varphi}, \boldsymbol{u}\rangle = \sum_{E\in\mathcal{T}_h} \int_E D_{\mathrm{DG}}\mathbf{u}\colon \mathbb{A}(\mathbf{X}, D_{\mathrm{DG}}\boldsymbol{\varphi})\colon D_{\mathrm{DG}}\delta\boldsymbol{\varphi}\ dV, \tag{21}$$

and $\mathbf{u}$ is another admissible variation to be solved for. Alternatively, $\mathbf{u}$ can be regarded as a displacement field with respect to the configuration of the body given by $\boldsymbol{\varphi}$. In the context of discontinuous Galerkin methods for linear problems, equation (20) is known as the primal formulation.

The current formulation possesses a number of salient features worth highlighting. For example, the resulting numerical algorithm always derives from a discrete variational principle analogous to that of the continuous problem. This has proved to be advantageous for the algorithmic analysis and mesh adaption in the context of nonlinear problems [37], and for the computation of configurational forces [21], such as the J–integral in fracture mechanics. Moreover, the second variation of a smooth scalar potential is always symmetric, and so is the matrix in equation (21).

Another distinguishing feature of the present framework is its flexibility for the design of different flavors of discontinuous Galerkin methods for nonlinear elasticity. Notice that we have not yet specified the numerical flux $\hat{v}$, given that any of the known numerical fluxes in the literature (see, e.g., [2]) can be adopted. It should be noted, however, that most discontinuous Galerkin discretizations need the specification of numerical fluxes for both the field and its derivative. By choosing only the form of $\hat{v}$ we automatically respect the variational structure of the original problem. Alternative approaches, in which the discontinuous Galerkin discretization is constructed directly from the Euler–Lagrange equations and both fluxes are chosen, need to satisfy additional compatibility conditions to derive from variations of a scalar potential.

Finally, a recurring source of concern in the adoption of discontinuous Galerkin methods stems for their often higher–computational cost. The present formulation contains only one

field, the deformation mapping, and hence exhibits a computational complexity comparable to that of conforming finite element methods. This is nicely illustrated by the numerical examples in section 6.4.

3.3. A choice of numerical fluxes

A particularly attractive choice for the numerical flux $\hat{v}$ is the one used in [22] for linear elasticity, in [5] for Navier-Stokes equations and in [9] for the scalar diffusion equation, known as the Bassi and Rebay numerical flux, after [5]. In this case we let $\hat{v}(\boldsymbol{\varphi}) = \hat{v}_0(\boldsymbol{\varphi}) + \hat{v}_\partial(\boldsymbol{\varphi})$, where

$$\hat{v}_0(\boldsymbol{\varphi}) = \begin{cases} \{\boldsymbol{\varphi}\} & \text{on } \Gamma^I \\ 0 & \text{on } \Gamma^d \\ 0 & \text{on } \Gamma^\tau \end{cases}, \qquad \hat{v}_\partial(\boldsymbol{\varphi}) = \begin{cases} 0 & \text{on } \Gamma^I \\ \overline{\boldsymbol{\varphi}} & \text{on } \Gamma^d \\ \boldsymbol{\varphi} & \text{on } \Gamma^\tau, \end{cases} \tag{22}$$

and the resulting D_{DG} operator is

$$D_{\mathrm{DG}}\boldsymbol{\varphi} = \nabla\boldsymbol{\varphi} + \mathbf{R}([\![\boldsymbol{\varphi}]\!]) - \mathbf{R}([\![\hat{v}_\partial(\boldsymbol{\varphi})]\!]), \tag{23}$$

since $\{\hat{v}(\boldsymbol{\varphi}) - \boldsymbol{\varphi}\} = \{\{\boldsymbol{\varphi}\} - \boldsymbol{\varphi}\} = 0$ and $[\![\{\boldsymbol{\varphi}\}]\!] = 0$ on Γ^I, while $[\![\hat{v}_0(\boldsymbol{\varphi})]\!] = 0$ on $\Gamma \setminus \Gamma^I$.

The numerical flux $\hat{v}_\partial$ is used to impose boundary conditions. If the discrete functional space V_h^d contains only functions that attain the prescribed value $\overline{\boldsymbol{\varphi}}$ on Γ^d, then $[\![\hat{v}(\boldsymbol{\varphi}) - \boldsymbol{\varphi}]\!] = 0$ on Γ^d, and the boundary conditions do not contribute to the value of $D_{\mathrm{DG}}\boldsymbol{\varphi}$. Alternatively, if functions in V_h^d can attain any value on Γ^d, then $\hat{v}_\partial$ is used to impose Dirichlet boundary conditions weakly. In our numerical examples we chose to adopt the latter.

3.4. A three–field variational principle

The formulation in the previous section can be recast into a three–field variational principle, with deformation gradients and first Piola–Kirchhoff stress tensors as additional independent variables. In fact, as we shall see, it is equivalent to an element–by–element Hu–Washizu variational principle. This ensues after enforcing equation (23) weakly, as in (16), with the first Piola–Kirchhoff stress tensor as the test function,

$$\begin{aligned} I_h^{\mathrm{HW}}&[\boldsymbol{\varphi}, \mathbf{F}, \mathbf{P}] \\ &= \int_{\mathcal{B}_0} W(\mathbf{X}, \mathbf{F})\ dV + \sum_{E \in \mathcal{T}_h} \int_E (\nabla\boldsymbol{\varphi} + \mathbf{R}([\![\boldsymbol{\varphi}]\!]) - \mathbf{R}([\![\hat{v}_\partial(\boldsymbol{\varphi})]\!]) - \mathbf{F}) : \mathbf{P}\ dV \\ &\quad - \int_{\partial_\tau \mathcal{B}_0} \overline{T} \cdot \boldsymbol{\varphi}\ dS \\ &= \sum_{E \in \mathcal{T}_h} \int_E [W(\mathbf{X}, \mathbf{F}) + (\nabla\boldsymbol{\varphi} - \mathbf{F}) : \mathbf{P}]\ dV - \int_\Gamma [\![\boldsymbol{\varphi}]\!] \otimes \mathbf{N} \colon \{\mathbf{P}\}\ dS \\ &\quad + \int_{\Gamma^d} \overline{\boldsymbol{\varphi}} \otimes \mathbf{N} \colon \mathbf{P}\ dS + \int_{\Gamma^\tau} \boldsymbol{\varphi} \otimes \mathbf{N} \colon \mathbf{P}\ dS - \int_{\partial_\tau \mathcal{B}_0} \overline{T} \cdot \boldsymbol{\varphi}\ dS \\ &= \sum_{E \in \mathcal{T}_h} I_E[\boldsymbol{\varphi}, \mathbf{F}, \mathbf{P}], \end{aligned} \tag{24}$$

where the elemental Hu-Washizu functionals I_E are given by

$$I_E[\boldsymbol{\varphi}, \mathbf{F}, \mathbf{P}] = \int_E \left[W(\mathbf{X}, \mathbf{F}) + (\nabla\boldsymbol{\varphi} - \mathbf{F}) : \mathbf{P} \right] \, dV - \int_{\partial E \cap \partial_\tau \mathcal{B}_0} \overline{T} \cdot \boldsymbol{\varphi} \, dS \\ - \int_{\partial E \setminus \partial \mathcal{B}_0} \frac{1}{2} \left(\boldsymbol{\varphi} - \boldsymbol{\varphi}^{\text{ext}} \right) \otimes \mathbf{N} \colon \mathbf{P} \, dS - \int_{\partial E \cap \partial_d \mathcal{B}_0} (\boldsymbol{\varphi} - \overline{\boldsymbol{\varphi}}) \otimes \mathbf{N} \colon \mathbf{P} \, dS. \quad (25)$$

With $\boldsymbol{\varphi}^{\text{ext}}$ we denote the value of $\boldsymbol{\varphi}$ across the element boundary ∂E. Each of the functionals I_E, obtained here by a rearrangement of (24), can instead be explicitly derived from an application of the Hu–Washizu functional (see, e.g., [22]) on each element. Care must be exercised though in not double counting element boundary contributions, and hence the origin of the $1/2$ factor when integrating on $\partial E \setminus \partial \mathcal{B}_0$.

The stress and strain fields are extracted from $W_h^{d\times d}$, while the deformation mapping is to be found in V_h^d. If, as assumed, $\nabla V_h^d \subseteq W_h^{d\times d}$, then the stationary points of I_h^{HW} are described by the following equations

$$0 = \int_E \left(\frac{\partial W}{\partial \mathbf{F}}(\mathbf{X}, \mathbf{F}) - \mathbf{P} \right) : \delta\mathbf{F} \, dV \quad (26)$$

$$0 = \nabla\boldsymbol{\varphi} + \mathbf{R}(\llbracket \boldsymbol{\varphi} \rrbracket) - \mathbf{R}(\llbracket \hat{v}_\partial(\boldsymbol{\varphi}) \rrbracket) - \mathbf{F} \quad (27)$$

$$0 = \sum_{E \in \mathcal{T}_h} \int_E D_{\text{DG}} \delta\boldsymbol{\varphi} \colon \mathbf{P} \, dV - \int_{\partial_\tau \mathcal{B}_0} \overline{T} \cdot \delta\boldsymbol{\varphi} \, dS \quad (28)$$

for all admissible variations $\delta\mathbf{F}$ and $\delta\boldsymbol{\varphi}$. As expected from the construction, we recover (17), while an immediate examination of equation (26) reveals that the discrete first Piola–Kirchhoff stress field is just the L^2–projection onto $W_h^{d\times d}$ of the constitutive equation. By replacing both equations into (28), we recover the Euler–Lagrange equation (19) from our one–field discrete variational principle.

For the sake of simplicity, we derived a three–field variational principle for the particular choice of numerical flux given in section 3.3. It is clear nonetheless that an analogous construction can be done for any choice of $\hat{v}$, and it provides an explicit way of creating a family of three–field variational principles, including the Hu–Washizu. Nevertheless, for computational efficiency the use of the equivalent one–field variational principle is much more attractive. For any of these principles, the stress and strain fields can always be computed *a posteriori*, once the discrete deformation mapping is known.

3.5. Lifting operators

The objective in this section is to briefly describe and explain the behavior of the lifting operators. We begin by recalling some of the important properties extensively described elsewhere, see e.g. [22, 2]. An insightful decomposition is obtained by defining for faces $e \in \Gamma$ and $e' \in \Gamma^I$ the operators $\mathbf{R}^e : L^2(e) \mapsto W_h^d$ and $\mathbf{L}^{e'} : L^2(e') \mapsto W_h^d$ that satisfy

$$\int_{\mathcal{B}_0} \mathbf{R}^e(v) \cdot \mathbf{z} \, dV = -\int_e v \otimes \mathbf{N} \cdot \{\mathbf{z}\} \, dS \qquad \int_{\mathcal{B}_0} \mathbf{L}^{e'}(v) \cdot \mathbf{z} \, dV = -\int_{e'} v \otimes \mathbf{N} \cdot \llbracket \mathbf{z} \rrbracket \, dS, \quad (29)$$

for all $\mathbf{z} \in W_h^d$. Evidently we have that $\mathbf{R} = \sum_{e\in\Gamma} \mathbf{R}^e$ and $\mathbf{L} = \sum_{e'\in\Gamma^I} \mathbf{L}^{e'}$. As in section 3.1, these operators are trivially extended to the case in which D_{DG} is computed for a vector field,

and we shall employ the same notation for both cases. It is immediate to see that $\mathbf{R}^e$ and $\mathbf{L}^e$ are different from zero only in elements E^+ and E^-, such that $E^+ \cap E^- = e$, and that

$$\mathbf{R}^e(v) = \mp 2\mathbf{L}^e(v) \qquad \text{in } E^{\pm}. \tag{30}$$

An essential property of lifting operators is that

$$\mathbf{R}^e(\llbracket v \rrbracket) = 0 \text{ in } \mathcal{B}_0 \iff \llbracket v \rrbracket = 0 \text{ on } e \tag{31}$$

for all $v \in V_h$ and all $e \in \Gamma$. The fact that if $\llbracket v \rrbracket = 0$ on e then $\mathbf{R}^e(\llbracket v \rrbracket) = 0$ is trivial. For the converse, consider a special test function $\mathbf{z} \in W_h^d$, such that $\{\mathbf{z}\} \cdot \mathbf{N} = \llbracket v \rrbracket$ on e. Such a function exists, given that $V_h \subseteq W_h$, and $\|\mathbf{z}\|_{0,\mathcal{B}_0} \neq 0$ if $\llbracket v \rrbracket \neq 0$ on e. Here $\|\cdot\|_{0,\Omega}$ indicates the L^2–norm over a set Ω. Thus,

$$\frac{1}{2}\|\llbracket v \rrbracket\|_{0,e}^2 = \left|\frac{1}{2}\int_e \llbracket v \rrbracket \cdot \llbracket v \rrbracket \; dS\right| = \left|\int_{\mathcal{B}_0} \mathbf{R}^e(\llbracket v \rrbracket) \cdot \mathbf{z} \; dV\right| \leq \|\mathbf{R}^e(\llbracket v \rrbracket)\|_{0,\mathcal{B}_0} \|\mathbf{z}\|_{0,\mathcal{B}_0} \tag{32}$$

Hence, it follows from equation (32) that if $\llbracket v \rrbracket \neq 0$ on e then $\mathbf{R}^e(\llbracket v \rrbracket) \neq 0$, or, that if $\mathbf{R}^e(\llbracket v \rrbracket) = 0$ then $\llbracket v \rrbracket = 0$ on e. Analogously, we have that

$$\mathbf{L}^{e'}(\{v\}) = 0 \iff \{v\} = 0 \text{ on } e' \tag{33}$$

for all $v \in V_h$ and all $e' \in \Gamma^I$, which follows immediately from equation (30) by considering $v' \in V_h$ such that $\{v\} = \llbracket v' \rrbracket$ on e. This property of the lifting operators is a direct consequence of the fact that for a quasi–uniform [8, p. 106] family of admissible subdivisions, in which all elements are affine equivalent [8, p. 80] to a finite number of reference elements, there exist constants $C^+, C^- > 0$ such that

$$C^- h^{1/2} \|\mathbf{R}^e(\llbracket v \rrbracket)\|_{0,\mathcal{B}_0} \leq \|\llbracket v \rrbracket\|_{0,e} \leq C^+ h^{1/2} \|\mathbf{R}^e(\llbracket v \rrbracket)\|_{0,\mathcal{B}_0} \tag{34}$$

for all $v \in V_h$, where h is a measure of the mesh fineness. The proof of this lemma can be found in several references, e.g., [22, 2].

4. STABILIZATION

The use of discontinuous fields across element boundaries may occasionally produce a linearized problem in which the associated bilinear form, equation (21), is coercive in the subspace of continuous functions in V_h^d, but fails to be so in all of V_h^d. This feature is also encountered in the unstressed linear elastic case, see [22], where a stabilization term was added to prevent this pathology from appearing.

Linearized nonlinear elasticity problems need not be coercive; in fact, some of the most interesting phenomena is observed precisely when coercivity is lost, e.g., buckling. A positive definite linearized elastic problem is associated with linear stability of the current configuration, with no incipient zero or negative energy modes. It is therefore unrealistic to expect positive definiteness of the linearized problem for each possible configuration; it does make sense, however, to request the discrete bilinear form (21) to be positive definite whenever the current configuration is linearly stable. In the following we show that, even though we are not yet able to fully comply with this request, we can substantially increase the stability range of the discontinuous Galerkin discretization by the addition of a suitable stabilization term.

There are several examples of stabilized methods in the literature (e.g., [9, 22, 40]). We discuss and analyze next the stabilization scheme we adopt for the nonlinear setting, which, additionally, preserves the variational framework of the problem. For simplicity we concentrate here in the particular choice of fluxes in section 3.3 ; a more general analysis should be possible with minor modifications.

The type of stabilization term considered here is a natural extension of the one used in [40] for linear elasticity. We modify the functional I_h in equation (18) by adding a stabilization term to obtain

$$I_h^\beta[\mathbf{v}] = I_h[\mathbf{v}] + \frac{\beta}{h}\int_\Gamma [\![\mathbf{v} - \hat{v}(\mathbf{v})]\!] \cdot [\![\mathbf{v} - \hat{v}(\mathbf{v})]\!]\, dS, \tag{35}$$

where β is some positive number, and h is a measure of the mesh fineness. It will be evident from the forthcoming analysis that an equivalent stabilized formulation is obtained from equation (34) in the form

$$I_h[\mathbf{v}] + \beta \sum_{e\in\Gamma}\int_{\mathcal{B}_0} \mathbf{R}^e([\![\mathbf{v} - \hat{v}(\mathbf{v})]\!]) \cdot \mathbf{R}^e([\![\mathbf{v} - \hat{v}(\mathbf{v})]\!])\, dV, \tag{36}$$

which was proposed in [9] for the scalar diffusion equation, and used in [22] for the linear elasticity case. We adopt the formulation in equation (35) for the numerical examples, but the coercivity analysis below applies to either one. Notice that either term vanishes for continuous functions in V_h^d that satisfy the boundary conditions on $\partial_d\mathcal{B}_0$. Also, as written, the stabilization parameter fails to be nondimensional; it has the units of the elastic moduli. Once a specific problem is chosen, β can be nondimensionalized accordingly.

In the following we restrict ourselves to $\mathcal{B}_0 \subset \mathbb{R}^d$ with $d = 2, 3$ so that some results in [25] are directly applicable; a more general treatment may be possible. Throughout this section we will consider a deformed configuration $\boldsymbol{\varphi} \in V_h^d$, with corresponding DG–derivative $\mathbf{F} = D_{\mathrm{DG}}\boldsymbol{\varphi} \in W_h^{d\times d}$. Furthermore, we assume that there exists $\epsilon > 0$ such that $\det \mathbf{F} > \epsilon$ in $\cup_{E\in\mathcal{T}_h} E$. The associated bilinear form of the linearized problem at $\boldsymbol{\varphi}$ is

$$\langle \delta^2 I_h^\beta[\boldsymbol{\varphi}], \mathbf{u}, \boldsymbol{v}\rangle = \sum_{E\in\mathcal{T}_h}\int_E D_{\mathrm{DG}}\mathbf{u} \colon \mathbb{A}(\mathbf{X}, \mathbf{F}) \colon D_{\mathrm{DG}}\mathbf{v}\, dV + \frac{\beta}{h}\int_{\Gamma\setminus\Gamma_\tau} [\![\mathbf{u}]\!] \cdot [\![\mathbf{v}]\!]\, dS, \tag{37}$$

for any $\mathbf{u}, \mathbf{v} \in V_h^d$. The properties of this bilinear form are a direct consequence of the form of the first elasticity tensor $\mathbb{A}$, the key difficulties arising from the material frame indifference postulate on the strain energy density and possible material instabilities arising from a stressed linearized configuration. These are partially unveiled after rewriting the first term in the right hand side of equation (37) as follows

$$\sum_{E\in\mathcal{T}_h}\int_E \left(u_{i,j} + r_{ij}([\![\mathbf{u}]\!])\right) \mathrm{a}_{ijkl} \left(v_{k,l} + r_{ij}([\![\mathbf{v}]\!])\right)\, dV, \tag{38}$$

where we introduced the *spatial lifting operators* as

$$\mathbf{r}(\cdot) = \mathbf{R}(\cdot)\cdot\mathbf{F}^{-1}$$

and the *spatial displacement gradient*

$$\nabla_{\mathbf{F}}\mathbf{u} = \nabla\mathbf{u}\cdot\mathbf{F}^{-1}$$

of a displacement field $\mathbf{u}$, or, in indicial notation, $u_{i,j} = u_{i,J}F^{-1}_{Jj}$. In equation (38) we used one of two more elasticity tensors relevant for the subsequent analysis, namely, $\mathbf{a}$ and $\mathbf{c}$, where

$$c_{ijkl}(\mathbf{X},\mathbf{F}) = 2\mathbb{C}_{IJKL}(\mathbf{X},\mathbf{F}^{\mathsf{T}}\mathbf{F})F_{iI}F_{jJ}F_{kK}F_{lL} \tag{39}$$

$$\begin{aligned}\mathrm{a}_{ijkl}(\mathbf{X},\mathbf{F}) &= A_{iJkL}(\mathbf{X},\mathbf{F})F_{jJ}F_{lL} \\ &= c_{ijkl}(\mathbf{X},\mathbf{F}) + \tau_{jl}(\mathbf{X},\mathbf{F})\delta_{ik}.\end{aligned} \tag{40}$$

Here $\boldsymbol{\tau}$ is the Kirchhoff stress tensor, which is symmetric. It follows from these definitions that $\mathbf{a}$ has only major symmetries, while $\mathbf{c}$ has both major and minor symmetries, a direct consequence of the material frame indifference postulate. Consequently, $\mathrm{w}_{ij}\mathrm{a}_{ijkl}\mathrm{w}_{kl} = \tau_{jl}\mathrm{w}_{ij}\mathrm{w}_{il}$ for any skew–symmetric tensor $\mathbf{w}$, which can be negative definite when $\boldsymbol{\tau}$ has negative eigenvalues, i.e., under compression.

For the upcoming discussion, it is convenient to define the *spatial lifting operators*

$$\mathbf{r}^e(\cdot) = \mathbf{R}^e(\cdot)\cdot\mathbf{F}^{-1} \text{ and } \mathbf{r}^{e,s} = \frac{1}{2}\left(\mathbf{r}^e + [\mathbf{r}^e]^{\mathsf{T}}\right),$$

and the symmetric part of the spatial displacement field

$$\nabla_{\mathbf{F},s}\mathbf{u} = \frac{1}{2}\left(\nabla\mathbf{u}\cdot\mathbf{F}^{-1} + \mathbf{F}^{-\mathsf{T}}\cdot\nabla\mathbf{u}^{\mathsf{T}}\right).$$

Also, let

$$[H^1_\partial(\mathcal{B}_0)]^d = \left\{\mathbf{u}\in[H^1(\mathcal{B}_0)]^d \mid \mathbf{u}|_{\partial_d\mathcal{B}_0} = 0\right\}, \tag{41}$$

where, as assumed, $\partial_d\mathcal{B}_0$ has positive $\mathcal{H}^{d-1}$ measure. We will prove in Lemma 4.2 that the functionals $|\!|\!|\cdot|\!|\!|_{\mathbf{F},s} : V^d_h + [H^1_\partial(\mathcal{B}_0)]^d \mapsto \mathbb{R}$ and $|\!|\!|\cdot|\!|\!|_{\mathbf{F}} : V^d_h + [H^1_\partial(\mathcal{B}_0)]^d \mapsto \mathbb{R}$ given by

$$|\!|\!|\mathbf{u}|\!|\!|^2_{\mathbf{F},s} = \sum_{E\in\mathcal{T}_h}\|\nabla_{\mathbf{F},s}\mathbf{u}\|^2_{0,E} + \sum_{e\in\Gamma}\|\mathbf{r}^{e,s}(\llbracket\mathbf{u}\rrbracket)\|^2_{0,\mathcal{B}_0} \tag{42}$$

$$|\!|\!|\mathbf{u}|\!|\!|^2_{\mathbf{F}} = \sum_{E\in\mathcal{T}_h}\|\nabla_{\mathbf{F}}\mathbf{u}\|^2_{0,E} + \sum_{e\in\Gamma}\|\mathbf{r}^{e}(\llbracket\mathbf{u}\rrbracket)\|^2_{0,\mathcal{B}_0} \tag{43}$$

are norms in $V^d_h + [H^1_\partial(\mathcal{B}_0)]^d$. In particular, when $\mathbf{F}$ is the identity tensor, we recover the norms $|\!|\!|\cdot|\!|\!|_s$, $|\!|\!|\cdot|\!|\!|$ in $V^d_h + [H^1_\partial(\mathcal{B}_0)]^d$ from [22], used for the classical linear elastic case. In addition, in the same lemma we obtain that there exists a constant $k_1 > 0$ such that

$$k_1|\!|\!|\mathbf{u}|\!|\!|^2_{\mathbf{F}} \le |\!|\!|\mathbf{u}|\!|\!|^2_{\mathbf{F},s} \le |\!|\!|\mathbf{u}|\!|\!|^2_{\mathbf{F}}, \tag{44}$$

for all $[H^1_\partial(\mathcal{B}_0)]^d$. It therefore follows that, since V^d_h is finite dimensional, there exists a constant $k_{1h} > 0$ such that

$$k_{1h}|\!|\!|\mathbf{u}|\!|\!|^2_{\mathbf{F}} \le |\!|\!|\mathbf{u}|\!|\!|^2_{\mathbf{F},s} \le |\!|\!|\mathbf{u}|\!|\!|^2_{\mathbf{F}}, \tag{45}$$

for all $\mathbf{u}\in V^d_h$. Equation (45) can be regarded as a partial generalization of Korn's inequalities for functions in $\Pi_{E\in\mathcal{T}_h}[H^1(E)]^d$ independently proved by [22] and [7].

We discuss next some basic features of the linearized nonlinear elasticity problem. We illustrate the main ideas and deliberately obviate all technical assumptions. The linearized nonlinear elasticity problem consists of finding $\mathbf{u}\in[H^1(\mathcal{B}_0)]^d$ such that

$$\int_{\mathcal{B}_0} u_{i,J}A_{iJkL}v_{k,L}\,dV = \int_{\mathcal{B}_0} f_iv_i\,dV \tag{46}$$

for all $\mathbf{v} \in [H^1(\mathcal{B}_0)]^d$ given $\mathbf{f} \in [H_0^1(\mathcal{B})']^d$, and can be generally proved to have solutions if $\mathbb{A}$ is *strongly elliptic*, i.e.,

$$\mathbb{A}_{iJkL}\ \xi_i N_J \xi_k N_L \geq \epsilon\ \xi_i \xi_i N_J N_J \tag{47}$$

for all $\mathbf{X} \in \mathcal{B}_0$ and some constant $\epsilon > 0$, and for any vectors $\boldsymbol{\xi}, \mathbf{N} \in \mathbb{R}^d$ [23]. Strong ellipticity generally implies Garding's inequality, namely, that there exist constants $b_1, b_2 \geq 0$ such that

$$\int_{\mathcal{B}_0} u_{i,J} \mathbb{A}_{iJkL} u_{k,L}\ dV \geq b_1 \|\mathbf{u}\|_{1,\mathcal{B}_0}^2 - b_2 \|\mathbf{u}\|_{0,\mathcal{B}_0}^2, \tag{48}$$

for all $\mathbf{u} \in [H^1(\mathcal{B}_0)]^d$, see [23] and references therein. By a standard argument ([23]), it follows that the space of functions in $\mathbf{u} \in [H^1(\mathcal{B}_0)]^d$ for which the left hand side in equation (48) is nonpositive is finite dimensional. However, even after fixing displacements on $\partial_d \mathcal{B}_0$, the positive definiteness of the left hand side is not always assured. In fact, these are the buckling modes.

The definition of linearized stability for a given configuration follows naturally from the foregoing discussion, namely, there exists $b_3 > 0$ such that

$$\int_{\mathcal{B}_0} u_{i,J} A_{iJkL} u_{k,L}\ dV \geq b_3 \|\mathbf{u}\|_{1,\mathcal{B}_0}^2 \tag{49}$$

for all $\mathbf{u} \in [H^1(\mathcal{B}_0)]^d$. Although not true in general, under some conditions strong ellipticity does imply linearized stability; for example when $\mathbb{A}$ is constant through the domain and $\partial \mathcal{B}_0 = \partial_d \mathcal{B}_0$, see [23, p. 323].

The existence of necessary and sufficient conditions on $\mathbb{A}$, or $\mathbf{a}$, for linearized stability is apparently still an open question. From the foregoing discussion on the symmetries on $\mathbf{a}$, we cannot expect $\mathbf{a}$ to be positive semidefinite without ruling out many relevant configurations. This is in contrast with the unstressed linear elasticity problem, where $\mathrm{a}_{ijkl} = \mathrm{c}_{ijkl}$. In this case to obtain linearized stability it is customary to request the existence of $C_1 > 0$ such that

$$\mathrm{c}_{ijkl} g_{ij} g_{kl} \geq C_1 g_{ij}^s g_{ij}^s, \tag{50}$$

for all tensors $\mathbf{g} \in \mathbb{R}^{d \times d}$ and all $\mathbf{X} \in \mathbb{R}^d$, where $\mathbf{g}^s = (\mathbf{g} + \mathbf{g}^\mathsf{T})/2$, and then use Korn's inequality. As we shall illustrate through an example, it is somewhat restrictive to request condition (50) in the general linearized nonlinear elasticity problem. The elastic moduli $\mathbf{c}$ may not be positive semidefinite for symmetric tensors at some configuration; nevertheless, if the configuration is stressed, linear stability may follow anyhow. For instance, the strain energy density for a neohookean material extended to the compressible range is

$$W(\mathbf{F}) = \frac{\lambda}{2} \left(\log(\det \mathbf{F})\right)^2 - \mu \log(\det \mathbf{F}) + \frac{\mu}{2} \mathbf{F} \colon \mathbf{F}, \tag{51}$$

where $\lambda, \mu > 0$ are material constants. A straightforward computation yields the elastic moduli

$$\mathrm{a}_{ijkl} = \lambda \delta_{ij} \delta_{kl} + (\mu - \lambda \log(\det \mathbf{F}))\, \delta_{jk} \delta_{il} + \mu F_{jL} F_{lL} \delta_{ik} \tag{52}$$

$$c_{ijkl} = \lambda \delta_{ij} \delta_{kl} + (\mu - \lambda \log(\det \mathbf{F}))\, (\delta_{ik} \delta_{jl} + \delta_{il} \delta_{jk}) \tag{53}$$

Consider next hydrostatic compressions or expansions, i.e., $F_{iJ} = \alpha^{1/3} \delta_{iJ}$ with $\alpha > 0$. In this case we have for any tensor $\mathbf{g} \in \mathbb{R}^{3 \times 3}$ that

$$\mathrm{a}_{ijkl} g_{ij} g_{kl} = \lambda (g_{ii})^2 + \left(\mu(\alpha^{2/3} + 1) - \lambda \log \alpha\right) g_{ik}^s g_{ki}^s + \left(\mu(\alpha^{2/3} - 1) - \lambda \log \alpha\right) g_{ik}^w g_{ki}^w \tag{54}$$

$$c_{ijkl} g_{ij} g_{kl} = \lambda (g_{ii})^2 + (\mu - \lambda \log \alpha) 2 g_{kj}^s g_{kj}^s \tag{55}$$

where $\mathbf{g}^s$ and $\mathbf{g}^w$ are the symmetric and skew–symmetric parts of $\mathbf{g}$, respectively. It is simple to see then that if $\log\alpha > \mu/\lambda$ condition (50) is not longer satisfied, i.e., for large enough expansions $\mathbf{c}$ ceases to be positive definite for symmetric tensors. Nevertheless, the linearized problems may still be linearly stable. For example, if α is such that $(\log\alpha)/(\alpha^{2/3}-1) < \mu/\lambda < \log\alpha$, then $\mathbf{a}$ is positive definite for all tensors $\mathbf{g} \in \mathbb{R}^{3\times 3}$, and hence the linearized problem is linearly stable even though condition (50) does not hold.

In the following theorem, we propose a condition that sidesteps these difficulties and still guarantees linearized stability for the linearized continuous problem at a deformation $\boldsymbol{\varphi} \in V_h^d$, and the coercivity of the bilinear form for the stabilized discrete problem.

Theorem 4.1 (Coercivity) *Let $\boldsymbol{\varphi} \in V_h^d$ be a deformation mapping and $\mathbf{F} = D_{DG}\boldsymbol{\varphi}$ its DG–derivative, such that $\det\mathbf{F} > \epsilon$ for some $\epsilon > 0$, for all $\mathbf{X} \in \cup_{E\in\mathcal{T}_h} E$. Assume that there exist a constant $C_1 > 0$ such that*

$$\mathrm{a}_{ijkl}(\mathbf{X}, \mathbf{F}(\mathbf{X}))g_{ij}g_{kl} > C_1 g^s_{ij}g^s_{ij} - C_2 g_{ij}g_{ij} \tag{56}$$

for some constant C_2, for all tensors $\mathbf{g} \in \mathbb{R}^{d\times d}$ and for all $\mathbf{X} \in \cup_{E\in\mathcal{T}_h} E$, where $\mathbf{g}^s = (\mathbf{g}+\mathbf{g}^\mathsf{T})/2$. Additionally, assume that $k_1C_1 - C_2 > 0$, with $k_1 > 0$ the constant in equation (44). Then there exists $C > 0$ such that

$$\langle \delta^2 I_h[\boldsymbol{\varphi}], \mathbf{u}, \boldsymbol{u}\rangle > C\|\mathbf{u}\|^2_{\mathbf{F}} \tag{57}$$

for all $\mathbf{u} \in [H^1_\partial(\mathcal{B}_0)]^d$.

Furthermore, if $k_{1h}C_1 - C_2 > 0$ with $k_{1h} > 0$ the constant in equation (45), then there exists $C_h > 0$ such that

$$\langle \delta^2 I^\beta_h[\boldsymbol{\varphi}], \mathbf{u}, \boldsymbol{u}\rangle > C_h\|\mathbf{u}\|^2_{\mathbf{F}} \tag{58}$$

for all $\mathbf{u} \in V_h^d$, provided $\beta > 0$ is large enough.

Some remarks are pertinent here, before proceeding to the proof. Useful sufficient conditions for linearized stability on the elastic moduli $\mathbb{A}$, especially for compressed configurations, can hardly be based solely on the material constitutive behavior. Buckling is often geometrical in nature, and such condition needs to incorporate information about the current configuration of the body. In theorem 4.1 C_1 and C_2 carry information about the constitutive behavior of the material, while Korn's inequality constant k_1 carries information about the current shape of the body.

As hinted at the beginning of this section, theorem 4.1 does not guarantee the discrete linearized problem to be coercive in V_h^d even if the current configuration is linearly stable in $[H^1_\partial(\mathcal{B}_0)]^d$. This may be the case if, for example, $k_{1h}C_1 - C_2 < 0 < k_1C_1 - C_2$. Then, the discrete problem may not be coercive for any β. With no added stabilization, however, the range of stable configurations for the discrete problem would be severely reduced. This particular problem is not found when utilizing traditional conforming finite element discretizations, in lieu of discontinuous Galerkin, since the discrete spaces are just subspaces of $[H^1_\partial(\mathcal{B}_0)]^d$.

The proof of theorem 4.1 proceeds by first showing that both $\|\cdot\|_{\mathbf{F}}$ and $\|\cdot\|_{\mathbf{F},s}$ are norms in $V_h^d + [H^1_\partial(\mathcal{B}_0)]^d$. This is done in the following two lemmas.

Lemma 4.1. *Let $\mathbf{F} \in W_h^{d\times d}$ be such that $\det\mathbf{F} > \epsilon$ for some $\epsilon > 0$, for all $\mathbf{X} \in \cup_{E\in\mathcal{T}_h} E$. There exists a constant $k_2 > 0$ such that for all $\mathbf{u} \in V_h^d$ and any $e \in \mathcal{T}_h$*

$$k_2\left\|\mathbf{R}^e([\![\mathbf{u}]\!])\cdot\mathbf{F}^{-1}\right\|_{0,\mathcal{B}_0} \le \frac{1}{2}\left\|\mathbf{R}^e([\![\mathbf{u}]\!])\cdot\mathbf{F}^{-1} + \mathbf{F}^{-\mathsf{T}}\cdot[\mathbf{R}^e([\![\mathbf{u}]\!])]^\mathsf{T}\right\|_{0,\mathcal{B}_0} \le \left\|\mathbf{R}^e([\![\mathbf{u}]\!])\cdot\mathbf{F}^{-1}\right\|_{0,\mathcal{B}_0}$$

or, alternatively,

$$k_2 \left\|\mathbf{r}^e(\llbracket \mathbf{u} \rrbracket)\right\|_{0,\mathcal{B}_0} \leq \left\|\mathbf{r}^{e,s}(\llbracket \mathbf{u} \rrbracket)\right\|_{0,\mathcal{B}_0} \leq \left\|\mathbf{r}^e(\llbracket \mathbf{u} \rrbracket)\right\|_{0,\mathcal{B}_0} \tag{59}$$

Proof. It is immediate to see that $\left\|\mathbf{r}^{e,s}(\llbracket \mathbf{u} \rrbracket)\right\|_{0,\mathcal{B}_0} \leq \left\|\mathbf{r}^e(\llbracket \mathbf{u} \rrbracket)\right\|_{0,\mathcal{B}_0}$. For the left inequality we assume that $\llbracket \mathbf{u} \rrbracket \neq 0$, which corresponds to the nontrivial case. We consider first a face $e \in \mathcal{T}_h$ with normal $\mathbf{N}$. Let $\mathbf{T} \in \mathbb{R}^d$ be such that $\mathbf{T} \cdot \mathbf{N} = 0$, and consider test functions of the form $\mathbf{z} = \mathbf{T} \otimes \mathbf{w}$, for any $\mathbf{w} \in W_h^d$; clearly $\mathbf{z} \in W_h^{d \times d}$. It follows from the definition of $\mathbf{R}^e$ that

$$0 = \int_e (\llbracket \mathbf{u} \rrbracket \otimes \mathbf{N}) \cdot (\mathbf{T} \otimes \{\mathbf{w}\}) \, dS = \int_{\mathcal{B}_0} \mathbf{w} \cdot \mathbf{R}^e(\llbracket \mathbf{u} \rrbracket) \cdot \mathbf{T} \, dV \tag{60}$$

for all $\mathbf{w} \in W_h^d$. Consequently $\mathbf{R}^e(\llbracket \mathbf{u} \rrbracket) \cdot \mathbf{T} = 0$ in $\mathcal{B}_0$. Since this holds for any $\mathbf{T}$ such that $\mathbf{T} \cdot \mathbf{N} = 0$, we get that $\mathbf{R}^e(\llbracket \mathbf{u} \rrbracket) = \boldsymbol{\rho} \otimes \mathbf{N}$, with $\boldsymbol{\rho} \in W_h^d$. Alternatively, $\mathbf{r}^e(\llbracket \mathbf{u} \rrbracket) = \mathbf{R}^e(\llbracket \mathbf{u} \rrbracket) \cdot \mathbf{F}^{-1} = \boldsymbol{\rho} \otimes \left(\mathbf{F}^{-\mathsf{T}} \cdot \mathbf{N}\right)$, and $\left(\mathbf{F}^{-\mathsf{T}} \cdot \mathbf{N}\right) \neq 0$ because $\mathbf{F}$ is invertible. Notice that $\boldsymbol{\rho} = 0$ if and only if $\llbracket \mathbf{u} \rrbracket = 0$, because of (31).

However, a tensor of the form $\mathbf{q} \otimes \mathbf{n}$, with $\mathbf{q}, \mathbf{n} \in \mathbb{R}^d$, $\mathbf{n} \neq 0 \neq \mathbf{q}$, cannot be skew–symmetric. To see this, assume that $\mathbf{q} \otimes \mathbf{n} = -\mathbf{n} \otimes \mathbf{q}$. It follows that $\mathbf{q} = -\mathbf{n}(\mathbf{q} \cdot \mathbf{n})$, and hence that $\mathbf{q} \cdot \mathbf{n} = -\mathbf{q} \cdot \mathbf{n}$. But then $\mathbf{q} \cdot \mathbf{n} = 0$, and consequently $\mathbf{q} = 0$, which contradicts the hypothesis.

We conclude then that $\mathbf{r}^e(\llbracket \mathbf{u} \rrbracket)$ cannot be skew–symmetric, or $\left\|\mathbf{r}^{e,s}(\llbracket \mathbf{u} \rrbracket)\right\|_{0,\mathcal{B}_0}^2 > 0$. Therefore, there exists $C_e > 0$ such that the quotient $\left\|\mathbf{r}^{e,s}(\llbracket \mathbf{u} \rrbracket)\right\|_{0,\mathcal{B}_0}^2 / \left\|\mathbf{r}^e(\llbracket \mathbf{u} \rrbracket)\right\|_{0,\mathcal{B}_0}^2 \geq C_e > 0$ whenever $\llbracket \mathbf{u} \rrbracket \neq 0$. Since there are only a finite number of faces, we can choose $C > 0$ such that $C_e > C$ for all $e \in \mathcal{T}_h$, and the lemma is proved. □

Lemma 4.2 (F–norms and Korn's inequality) *Let $\mathbf{F} \in W_h^{d \times d}$ be such that $\det \mathbf{F} > \epsilon$ for some $\epsilon > 0$, for all $\mathbf{X} \in \cup_{E \in \mathcal{T}_h} E$. Then $\|\!|\cdot|\!\|_{\mathbf{F},s}$ and $|\!|\!|\cdot|\!|\!|_{\mathbf{F}}$ are norms in $V_h^d + [H_\partial^1(\mathcal{B}_0)]^d$. Furthermore, there exists a constant $k_1 > 0$ such that*

$$k_1 |\!|\!|\mathbf{u}|\!|\!|_{\mathbf{F}}^2 \leq \|\!|\mathbf{u}|\!|_{\mathbf{F},s}^2 \leq |\!|\!|\mathbf{u}|\!|\!|_{\mathbf{F}}^2, \tag{61}$$

for all $\mathbf{u} \in [H_\partial^1(\mathcal{B}_0)]^d$.

Proof. We will prove first that

$$\|\!|\mathbf{u}|\!|_{\mathbf{F},s} = 0 \iff \mathbf{u} = 0, \tag{62}$$

for any $\mathbf{u} \in V_h^d + [H_\partial^1(\mathcal{B}_0)]^d$. It is clear that if $\mathbf{u} = 0$ then $\|\!|\mathbf{u}|\!|_{\mathbf{F},s} = 0$. Assume then that $\|\!|\mathbf{u}|\!|_{\mathbf{F},s} = 0$. Let $\mathbf{u} = \mathbf{u}_1 + \mathbf{u}_2$, with $\mathbf{u}_1 \in [H_\partial^1(\mathcal{B}_0)]^d$ and $\mathbf{u}_2 \in V_h^d$. Of course, $\|\llbracket \mathbf{u}_1 \rrbracket\|_{0,e} = 0$ on any face e. It follows then from Lemma 4.1 that $\mathbf{R}^e(\llbracket \mathbf{u}_2 \rrbracket) \cdot \mathbf{F}^{-1} = 0$, and since $\mathbf{F}$ is invertible, $\mathbf{R}^e(\llbracket \mathbf{u}_2 \rrbracket) = 0$, and hence $\llbracket \mathbf{u}_2 \rrbracket = 0$ on Γ. Therefore, we have that $\|\llbracket \mathbf{u} \rrbracket\|_{0,e} = 0$ for any face $e \in \Gamma$, and from [31, Theorem 1.3] we get that $\mathbf{u} \in [H_\partial^1(\mathcal{B}_0)]^d$.

Next we use theorem 4.3 in [25], which states that since $\mathbf{u} \in [H^1(E)]^d$ and $\mathbf{F}$ is smooth in the interior of each element E,

$$\left\|\nabla \mathbf{u} \cdot \mathbf{F}^{-1} + \mathbf{F}^{-\mathsf{T}} \cdot \nabla \mathbf{u}^{\mathsf{T}}\right\|_{0,E} = 0 \iff \mathbf{u} = 0 \text{ in } E \tag{63}$$

provided that $\mathbf{u} = 0$ on at least one face $e \in \partial E$. We use this fact in every element in the mesh, starting with those with faces in $\partial \mathcal{B}_0$ and moving inward. More precisely, since $\llbracket \mathbf{u} \rrbracket = 0$ on Γ, it follows that $\mathbf{u} = 0$ on $\Gamma^d \cup \Gamma^\tau$. Then, from equation (63), it follows that $\mathbf{u} = 0$ in any element in $S_0 = \{E \in \mathcal{B}_0 \mid |\partial E \cap \partial \mathcal{B}_0| > 0\}$, and hence $\mathbf{u} = 0$ in $\gamma_0 = \cup_{E \in S_0} \partial E$. Similarly, for $n \in \mathbb{N}$, let $S_n = \{E \in \mathcal{B}_0 \mid |\partial E \cap \gamma_{n-1}| > 0\}$ and $\gamma_n = \cup_{E \in S_n} \partial E$. It follows by induction

that $\mathbf{u} = 0$ in S_n, for any $n \in \mathbb{N}$. Since the interior of $\mathcal{B}_0$ was assumed to be connected, any element $E \in S_n$ for some n large enough, and hence $\mathbf{u} = 0$ for all $E \in \mathcal{T}_h$. Equation (62) is therefore satisfied, the only nontrivial result to show that $\|\!| \cdot |\!\|_{\mathbf{F},s}$ is a norm in $V_h^d + [H^1_\partial(\mathcal{B}_0)]^d$. Likewise, from $\|\!|\mathbf{u}|\!\|_{\mathbf{F}} = 0$ we get that $\mathbf{u} \in [H^1_\partial(\mathcal{B}_0)]^d$. Since $\mathbf{F}$ and $\mathbf{F}^{-1}$ are bounded in $\mathcal{B}_0$ we conclude that there exist constants $C^+, C^- > 0$ such that $C^-\|\!|\mathbf{u}|\!\|_{\mathbf{F}} \leq \|\mathbf{u}\|_{1,\mathcal{B}_0} \leq C^+\|\!|\mathbf{u}|\!\|_{\mathbf{F}}$ for all $\mathbf{u} \in [H^1_\partial(\mathcal{B}_0)]^d$, from where it follows that $\|\!| \cdot |\!\|_{\mathbf{F}}$ is a norm in $V_h^d + [H^1_\partial(\mathcal{B}_0)]^d$.

It remains to prove equation (61), which cannot be strictly obtained from the results in [25], because $\mathbf{F}$ is not continuous in $\mathcal{B}_0$. However, the result is readily obtained by using Corollary 4.7 in [25] and the fact that $\|\!| \cdot |\!\|_{\mathbf{F},s}$ is a norm in $[H^1_\partial(\mathcal{B}_0)]^d$ in the proof of Theorem 4.10 in the aforementioned reference. For completeness, we detail it below.

We proceed in a standard way, by contradiction. Assume that there exists a sequence $\mathbf{u}_n \in [H^1_\partial(\mathcal{B}_0)]^d$ such that

$$\|\mathbf{u}_n\|_{1,\mathcal{B}_0} = 1, \qquad \text{but } \|\!|\mathbf{u}_n|\!\|_{\mathbf{F},s} \longrightarrow 0$$

By the Rellich compact embedding theorem there exists a subsequence again denoted $\mathbf{u}_n$ and $\mathbf{u} \in [H^1_\partial(\mathcal{B}_0)]^d$ such that $\mathbf{u}_n \rightharpoonup \mathbf{u}$ in $[H^1(\mathcal{B}_0)]^d$, $\mathbf{u}_n \to \mathbf{u}$ in $[L^2(\mathcal{B}_0)]^d$. The convexity of the map $\mathbf{U} \mapsto |\mathbf{U} \cdot \mathbf{F}^{-1} + \mathbf{F}^{-\mathsf{T}} \cdot \mathbf{U}^{\mathsf{T}}|^2$, for any $\mathbf{U} \in \mathbb{R}^{d\times d}$ at any $\mathbf{X} \in \mathcal{B}_0$, implies the weak lower semicontinuity of $\|\!| \cdot |\!\|_{\mathbf{F},s}$ and therefore

$$0 = \liminf_{n\to\infty} \|\!|\mathbf{u}_n|\!\|_{\mathbf{F},s} \geq \|\!|\mathbf{u}|\!\|_{\mathbf{F},s},$$

from where it follows that $\mathbf{u} = 0$.

Corollary 4.7 in [25] asserts that because $\mathbf{F}^{-1}$ is continuous in each element $E \in \mathcal{T}_h$ then

$$\|\nabla_{\mathbf{F},s}\mathbf{u}\|^2_{0,E} + \|\mathbf{u}\|^2_{0,E}$$

is a norm on $[H^1(E)]^d$ equivalent to the $\|\cdot\|_{1,E}$ norm. From

$$\begin{aligned}\|\!|\mathbf{u}_n - \mathbf{u}_m|\!\|_{\mathbf{F},s} + \|\mathbf{u}_n - \mathbf{u}_m\|_{0,\mathcal{B}_0} &= \sum_{E\in\mathcal{T}_h} \left(\|\nabla_{\mathbf{F},s}(\mathbf{u}_n - \mathbf{u}_m)\|^2_{0,E} + \|\mathbf{u}_n - \mathbf{u}_m\|^2_{0,E}\right) \\ &\leq \|\!|\mathbf{u}_n|\!\|_{\mathbf{F},s} + \|\!|\mathbf{u}_m|\!\|_{\mathbf{F},s} + \|\mathbf{u}_n - \mathbf{u}_m\|_{0,\mathcal{B}_0}\end{aligned}$$

we obtain that $\mathbf{u}_n$ is a Cauchy sequence in $[H^1(\mathcal{B}_0)]^d$. Consequently, $\mathbf{u}_n \to \mathbf{u}$ strongly in $[H^1(\mathcal{B}_0)]^d$ and $\|\mathbf{u}\|_{1,\mathcal{B}_0} = 1$, in contrast to $\mathbf{u} = 0$.

Since $C^-\|\!|\mathbf{u}_n|\!\|_{\mathbf{F}} \leq \|\mathbf{u}_n\|_{1,\mathcal{B}_0}$, it follows that there exists a constant $k_1 > 0$ such that

$$k_1\|\!|\mathbf{u}|\!\|_{\mathbf{F}} \leq \frac{k_1}{C^-}\|\mathbf{u}\|_{1,\mathcal{B}_0} \leq \|\!|\mathbf{u}|\!\|_{\mathbf{F},s}$$

□

Proof. [Theorem 4.1]

We prove first the linear stability of the continuous problem, equation (57). This is straightforward, namely, for $\mathbf{u} \in [H^1_\partial(\mathcal{B}_0)]^d$

$$\langle \delta^2 I_h[\boldsymbol{\varphi}], \mathbf{u}, \mathbf{u}\rangle \geq C_1 \sum_{E\in\mathcal{T}_h} \|\nabla_{\mathbf{F},s}\mathbf{u}\|^2_{0,E} - C_2 \sum_{E\in\mathcal{T}_h} \|\nabla_{\mathbf{F}}\mathbf{u}\|^2_{0,E} \tag{64}$$

$$\geq (k_1C_1 - C_2)\|\!|\mathbf{u}|\!\|^2_{\mathbf{F}}, \tag{65}$$

and since by hypothesis $k_1C_1 - C_2 > 0$, equation (57) follows.

For the discrete stability we will need the following inequalities. First, a consequence of equation (34),

$$\frac{\beta}{h}\sum_{e\in\Gamma}\int_e [\![\mathbf{u}]\!]\cdot[\![\mathbf{u}]\!]\; dS \geq \beta\; k_3 \sum_{e\in\Gamma}\|\mathbf{R}^e([\![\mathbf{u}]\!])\|^2_{0,\mathcal{B}_0} \geq \beta\; k_4 \sum_{e\in\Gamma}\|\mathbf{r}^e([\![\mathbf{u}]\!])\|^2_{0,\mathcal{B}_0}, \tag{66}$$

for some constants $k_3 > 0$ and $k_4 > 0$, and where we used the fact that $\mathbf{F}$ is invertible. The second inequality is for tensor fields $\mathbf{A}, \mathbf{B}\colon E \mapsto \mathbb{R}^{d\times d}$,

$$\begin{aligned}\|\mathbf{A}+\mathbf{B}\|^2_{0,E} &= \int_E (\mathbf{A}+\mathbf{B})\colon(\mathbf{A}+\mathbf{B})\; dV = \|\mathbf{A}\|^2_{0,E} + \|\mathbf{B}\|^2_{0,E} + \int_E 2\mathbf{A}\colon\mathbf{B}\; dV \\ &\geq \|\mathbf{A}\|^2_{0,E} + \|\mathbf{B}\|^2_{0,E} - \int_E \left(\xi\mathbf{A}\colon\mathbf{A} + \frac{1}{\xi}\,\mathbf{B}\colon\mathbf{B}\right)\; dV \\ &\geq (1-\xi)\|\mathbf{A}\|^2_{0,E} + (1-\frac{1}{\xi})\|\mathbf{B}\|^2_{0,E}\end{aligned} \tag{67}$$

for any $\xi > 0$, and any element E. In this derivation we used Young's inequality, namely, $2|ab| \leq \xi a^2 + b^2/\xi$, for all $a, b \in \mathbb{R}$.

Let $\overline{C}_2 = \max\{C_2, 0\}$. Next, by taking $g_{ij} = u_{i,j} + r_{ij}([\![\mathbf{u}]\!])$ for all $\mathbf{X} \in \cup_{E\in\mathcal{T}_h} E$, and integrating inequality (56) over every element we obtain

$$\langle \delta^2 I_h^\beta[\boldsymbol{\varphi}], \mathbf{u}, \mathbf{u}\rangle \geq$$

$$\begin{aligned}&\geq C_1 \sum_{E\in\mathcal{T}_h}\|\nabla_{\mathbf{F},s}\mathbf{u} + \sum_{e\in\partial E}\mathbf{r}^{e,s}([\![\mathbf{u}]\!])\|^2_{0,E} - C_2\sum_{E\in\mathcal{T}_h}\|\nabla_{\mathbf{F}}\mathbf{u} + \sum_{e\in\partial E}\mathbf{r}^{e}([\![\mathbf{u}]\!])\|^2_{0,E} \\ &\quad + \beta\; k_4\sum_{e\in\Gamma}\|\mathbf{r}^e([\![\mathbf{u}]\!])\|^2_{0,\mathcal{B}_0}\end{aligned} \tag{68}$$

$$\begin{aligned}&\geq C_1 \sum_{E\in\mathcal{T}_h}\left[(1-\xi)\|\nabla_{\mathbf{F},s}\mathbf{u}\|^2_{0,E} + \left(1-\frac{1}{\xi}\right)\|\sum_{e\in\partial E}\mathbf{r}^{e,s}([\![\mathbf{u}]\!])\|^2_{0,E}\right] \\ &\quad - \;\overline{C}_2\sum_{E\in\mathcal{T}_h}\left[\|\nabla_{\mathbf{F}}\mathbf{u}\|^2_{0,E} + \|\sum_{e\in\partial E}\mathbf{r}^{e}([\![\mathbf{u}]\!])\|^2_{0,E}\right] + \beta\; k_4\sum_{e\in\Gamma}\|\mathbf{r}^{e,s}([\![\mathbf{u}]\!])\|^2_{0,\mathcal{B}_0}\end{aligned} \tag{69}$$

$$\geq C_1\left[(1-\xi)\sum_{E\in\mathcal{T}_h}\|\nabla_{\mathbf{F},s}\mathbf{u}\|^2_{0,E} + \left(1-\frac{1}{\xi}+\beta\;\frac{k_4}{C_1}\right)\sum_{e\in\Gamma}\|\mathbf{r}^{e,s}([\![\mathbf{u}]\!])\|^2_{0,\mathcal{B}_0}\right] - \;\overline{C}_2\|\mathbf{u}\|^2_{\mathbf{F}} \tag{70}$$

$$\geq C_1\min\left\{(1-\xi), \left(1-\frac{1}{\xi}+\beta\;\frac{k_4}{C_1}\right)\right\}\|\mathbf{u}\|^2_{\mathbf{F},s} - \;\overline{C}_2\|\mathbf{u}\|^2_{\mathbf{F}} \tag{71}$$

$$\geq \left[k_{1h}C_1\min\left\{(1-\xi), \left(1-\frac{1}{\xi}+\beta\;\frac{k_4}{C_1}\right)\right\} - \;\overline{C}_2\right]\|\mathbf{u}\|^2_{\mathbf{F}}. \tag{72}$$

Equation (67) was used in (69), together with equation (66) and the triangle inequality. The latter was also used to obtain equation (70), while equation (45) was instrumental in obtaining (72).

Let $\alpha = (\overline{C}_2/(C_1k_{1h})$, clearly $0 \leq \alpha < 1$ by hypothesis. Then, if $\xi < 1-\alpha$ and

$$\beta > \left(\alpha - 1 + \frac{1}{\xi}\right)\frac{C_1}{k_4} \tag{73}$$

it is simple to check that the resulting bilinear form is coercive. Equivalently, if

$$\beta > \inf_{\xi\in(0,1-\alpha)} \left(\alpha - 1 + \frac{1}{\xi}\right)\frac{C_1}{k_4} = \left(\alpha - 1 + \frac{1}{1-\alpha}\right)\frac{C_1}{k_4}, \tag{74}$$

then the bilinear form is coercive in V_h^d, and the theorem is proved. □

Some remarks are pertinent here. We first note that the value of the coercivity constant in theorem 4.1 is a lower bound and not a tight estimate of the stability limit of the method. A simple modification of the derivation above leads to a larger lower bound for β when $C_2 < 0$. Anyhow, the theorem provides a way to estimate a sufficient value for the stabilization parameter β. Unfortunately, it appears to be a rather computationally expensive procedure, since all necessary constants C_1, C_2, k_4 and k_1 depend on the configuration $\boldsymbol{\varphi}$ at which the linearization is performed. It is perhaps useful to detail what the lower bound on β is for small departures from the stress–free configuration. In this case the geometric changes can be neglected, and hence consider k_{1h} as a constant, while the elastic moduli $\mathbf{c}$ remain positive definite for all symmetric tensors if the departures are small enough. For simplicity, we consider $\mathbf{c}$ constant as well. In this case $-C_2$ can be taken to be equal to the smallest eigenvalue $-t_{\max}$ of $\boldsymbol{\tau}$, the Kirchhoff stress. Therefore, when the maximum compressive stress $t_{\max}$ is small compared to the minimum stiffness of the material k_1C_1, we have from equation (74)

$$\beta \gtrapprox 2t_{\max}/(k_{1h}k_4),$$

which indicates that in this case β should be scaled with the maximum compressive stress $t_{\max}$, whenever $t_{\max} > 0$.

Finally, back to the example with a neohookean material in equation (51). Assume, for simplicity, that $\mu/\lambda < 3/2$ and let $\overline{\alpha}$ be such that $(\log\overline{\alpha})/(\overline{\alpha}^{2/3} - 1) = \mu/\lambda$. It is simple to see that if $\mu/\lambda < 3/2$ then $\overline{\alpha} > 1$. For the hydrostatic deformation case in equation (54) the optimal values of C_1 and C_2 satisfy

$$\begin{aligned} C_1 - C_2 &= \mu(1+\alpha^{2/3}) - \lambda\log\alpha \\ C_2 &= \mu(1-\alpha^{2/3}) + \lambda\log\alpha, \end{aligned} \tag{75}$$

or $C_1 = 2\mu > 0$ for any α. However, if $1 < \alpha < \overline{\alpha}$ then $C_2 > 0$, which demonstrates that the stability condition $k_1C_1 - C_2 > 0$ allows $\mathbf{a}$ in equation (54) to have negative eigenvalues and still have a linearly stable problem.

5. REMARKS ON IMPLEMENTATION

The complexity of implementation inherent to discontinuous Galerkin methods has been one of the major factors deterring their utilization. It is the objective of this section to outline basic considerations associated to the implementation of the class of methods described here, and to partially dismiss its apparent complexity.

The solution of nonlinear elasticity problems frequently involves, and requires, the solution of the sequence of configurations of the body under a prescribed loading path, also known as a quasistatic evolution. Given that multiple solutions for a given load are ubiquitous in these problems, the consideration of a loading path very often determines a natural sequence

of deformations for the body. We solve the nonlinear system of equations at each step with a Newton-Raphson method. Throughout this section the primary concern is to minimize the number of extra operations needed at each loading step and iteration of a nonlinear solver.

We consider a conforming finite element implementation as a baseline, and comment on the essential modifications to obtain the discontinuous Galerkin one. These include the pre–computation of the lifting operators and stabilization terms, and accounting for the larger elemental stiffness matrices and force vectors stemming from the use of the lifting operators.

A chief contribution to the computational complexity and cost of discontinuous Galerkin methods emanates from the need to loop over both elements and faces in the mesh; terms involving the numerical fluxes are computed during the latter. We circumvent this difficulty by regarding the lifting operators $\mathbf{R}$ as linear operators on V_h, and hence pre–computing their associated matrix representations. The loop over faces in the mesh is hereafter unnecessary; lifting operators needed for D_{DG} can be now computed at gauss points inside each element through the use of these matrices, see section 5.1. What makes this idea feasible is the size of the matrix representation of $\mathbf{R}^e$, which, due to the compact support of the operator, is a small constant independent of the dimension of V_h; see section 5.1. This practical consideration emboldens the use of a one–field formulation through the DG–derivative.

Likewise, a loop over faces is apparently needed when using the stabilization term in equation (35). Nonetheless, since the stabilization term is independent of the deformation of the body, it can easily be pre–computed as well, stored and just assembled into the stiffness matrix at each iteration of the nonlinear solver. A similar consideration holds for contributions stemming from Dirichlet boundary conditions, $\mathbf{R}(\llbracket \hat{v}_\partial(\boldsymbol{\varphi}) \rrbracket)$.

One of the most substantial deviations from traditional concepts in the implementation of the methods herein is the need for larger elemental stiffness matrices and force vectors, as also discussed in [9]. This originates in the dependence of the lifting operator inside an element on degrees of freedom in neighboring elements, a fact that can be checked by simple inspection. This is best illustrated in figure 1, where a discontinous Galerkin mesh of linear triangles is shown. To compute the lift of the inter–element jumps at any point inside the element shown in gray, we need the degrees of freedom in V_h at nodes 1, 2 and 3 *and* those at nodes 4 to 9. Hence the increased size of the elemental contributions to the global stiffness matrix and force vector. In practice, this results in modified elements with a larger connectivity, a rather simple way to merge these formulations into standard finite element codes. For example, in the case depicted in figure 1 the connectivity of the gray element includes nodes 1 to 9. It is noteworthy that, even though possibly different spaces V_h and W_h are considered, the presence of W_h is only encountered at the elemental level and never permeates to global operations, as reflected by the size of the elemental contributions.

Among other less important features, but still worth mentioning, we note that the stiffness matrix of each linearized problem is extremely sparse, with a fixed number of maximum nonzero entries per row; a brisk glance at figure 1 reveals that these only appear relating degrees of freedom of an element and those of any neighbor sharing a face. In conforming formulations it is enough for two elements to share at least a node to have nonzero entries relating their degrees of freedom. One of the downsides of the proposed implementation is that, with all the bookkeeping for pre–computed quantities and the possibility of using different shape functions for V_h and W_h, a larger amount of memory per degree of freedom needs to be allocated.

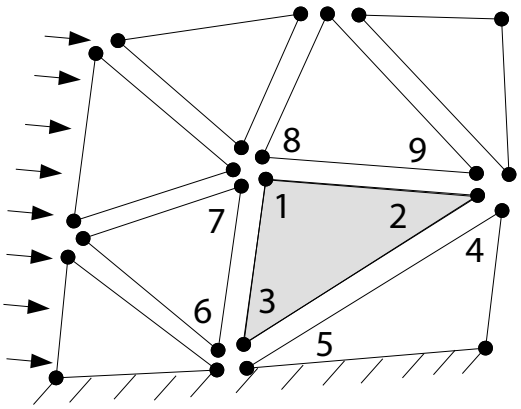

Figure 1. Example of a discontinuous Galerkin mesh composed of linear triangles. The degrees of freedom associated with the same node in the mesh, but different elements, have been depicted in different spatial positions to highlight the nature of the discretization.

5.1. Computation of the lifting operators

The formulation of a computationally efficient one–field discontinuous Galerkin method is feasible due to the use of the lifting operators. In the following we show how their matrix representation are constructed *a priori* and used within elemental calculations; these are pivotal tools to avoid unnecessary loops over all faces in the mesh.

The representation of the lifting operators with small matrices independently of the dimensions of V_h and W_h relies heavily on the choice of basis functions for these spaces. An appropriate choice in this case is provided by the standard basis functions for discontinuous Galerkin, which are constructed as follows. Let Q^E be an elemental basis function in V_h^E, the global basis function $Q \in V_h$ is such that $Q = Q^E$ in E and $Q = 0$ otherwise. Likewise for L, a basis function in W_h.

We next note that the lifting operator can be decomposed as $\mathbf{R} = \sum_{E \in \mathcal{T}_h} \mathbf{R}^E$, where $\mathbf{R}^E$ is the restriction of $\mathbf{R}$ to element E. The action of the restricted lifting operator $\mathbf{R}^E : L^2(\Gamma) \mapsto [W_h^E]^d$ on functions in V_h is succinctly summarized through its matrix representation in the chosen bases for V_h and W_h^E, namely,

$$\mathbf{R}^E(v_a Q_a) = v_a \mathbf{R}^E(Q_a) = v_a \mathbf{e}_i L_b^E R_{abi}^E, \tag{76}$$

where the matrix representation of $\mathbf{R}^E$ is given by R_{adi}^E, Q_a and L_b^E are basis functions in V_h and W_h^E, respectively, v_a are the components of a function in V_h, and $\mathbf{e}_i$ is a Cartesian basis in $\mathbb{R}^3$. Here and henceforth, the range of the summation over each repeated index is tacitly

understood. For example, in equation (76) sums over i range from 1 to d and a and b range through the number of degrees of freedom in V_h and W_h^E, respectively.

We show next that the number of nonzero entries in R^E_{abi} is a constant independent of the dimension of V_h. We recall that the support of $\mathbf{R}^e$ is included in the two elements that share face e. Therefore, $\mathbf{R}^E = \sum_{e\in\partial E} \mathbf{R}^e$ and $\mathbf{R}^E(Q_a) = 0$ if $a \notin C_E$, where C_E denotes the set of degrees of freedom of V_h in element E or any of its face–sharing neighbors. Accordingly, the only relevant entries of R^E_{abi} can be summarized in a matrix with dimensions of at most $\#C_E \times \dim W_h^E \times d$, a constant value independent of how large the space V_h is. For example, in the case shown in figure 1 in which linear triangles are used, the value of C_E for the gray element can be further reduced to include the degrees of freedom at nodes 1 to 9 only, i.e., from 12 to 9.

The values of R^E_{adi} effortlessly ensue from equation (15) by taking $v = Q_a$, $a \in C_E$, and $\mathbf{z} = \mathbf{e}_i L_f^E$, i.e.,

$$\underbrace{\int_E L_d^E(\mathbf{X}) L_f^E(\mathbf{X})\, dV}_{M^E_{fd}} \quad R^E_{adi} = -\int_\Gamma Q_a \mathbf{N}\cdot\mathbf{e}_i\{L_f^E\}\, dS = -\int_{\partial E} Q_a \mathbf{N}\cdot\mathbf{e}_i\{L_f^E\}\, dS, \tag{77}$$

where $\mathbf{M}^E$ is the mass matrix in W_h^E. Equation (77) possesses the remarkable property of involving only the inversion of an *elemental mass matrix* with a number of different right hand sides to compute the matrix representation of $\mathbf{R}^E$. The underlying reason for this is the block diagonal nature of the mass matrices for standard discontinuous Galerkin bases.

6. NUMERICAL EXAMPLES

We proceed next to study the performance of one of the proposed numerical methods through selected examples. Throughout this section we adopt the numerical fluxes in equation (22) and piecewise linear triangles and tetrahedra as elements. Also, for some of the examples we consider a non–polyhedral $\mathcal{B}_0$, which is approximated with a polyhedral mesh when discretized.

6.1. Behavior of the jumps

The first numerical example consists of an unstressed square elastic block with sides of length 10 m under plane strain. The material of the block is neohookean, i.e., its strain energy density is given in equation (51). Dirichlet boundary conditions are imposed on the top and bottom surface of the square, effectively displacing the upper surface up and to the right exactly one half its length, while keeping the bottom surface fixed. The vertical sides remain stress–free. The material properties are $\lambda = 1.43$ Pa and $\mu = 0.36$ Pa. It is also useful to define E and ν such that $\lambda = \nu E/((1+\nu)(1-2\nu))$ and $\mu = E/(2(1+\nu))$. At the linearized stress–free configuration E is the Young modulus of the material, and ν its Poisson ratio. For later use, we recall that if $\nu \to 0.5^-$ the material becomes nearly incompressible, since $\lambda/\mu \to \infty$. For this case, $E = 1$ Pa and $\nu = 0.4$.

The results of the simulations are shown in figure 2. To our surprise, no stabilization was needed here, i.e., $\beta = 0$. A close look at the results in the figure reveals that the solutions are effectively discontinuous, and the jumps are located predominantly in the areas with high shear. This is an interesting and, to some extent, expected result; linear triangles are incapable of

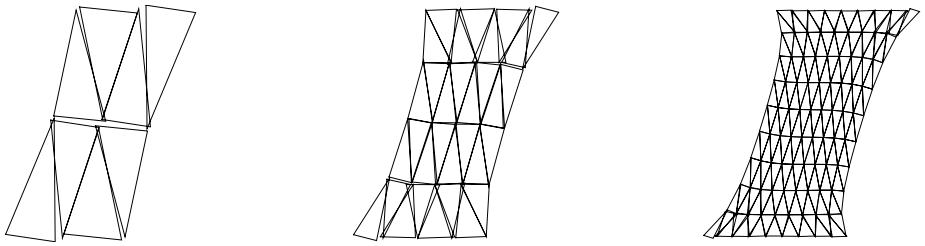

(a) Solution, 24 nodes (b) Solution, 96 nodes (c) Solution, 486 nodes

Figure 2. Deformation of a neohookean elastic block. Note that as the mesh is refined, the magnitude of the discontinuities steadily decreases.

bending, and therefore the best way for the method to approximate the deformation is through the presence of jumps. In addition, note that the magnitude of the discontinuities decreases as more degrees of freedom are used. In the stress–free linear elasticity case [22] it is seen that if the exact solution is smooth, then the jumps across element boundaries should asymptotically vanish as the mesh is refined. A similar statement is apparently valid in the nonlinear elastic case, as shown later in section 6.4. This type of situations are perhaps the most convenient tests for discontinuous Galerkin approximations, since the kinematic constraints imposed by the mesh can be easily relaxed through discontinuities. We discuss more about this in the next section.

6.2. Mesh-based kinematic constraints

In the following we study the square block of the previous section but under compression, the top boundary is quasistatically displaced downward. For this example we changed ν to be 0.45, and the mesh is composed of 216 nodes and 72 elements. In the absence of perturbations, the resulting deformation is expected to be completely symmetric with respect to a vertical axis through the center of the square. From figure 3(a), this is certainly the case for discontinuous Galerkin. Stabilization is needed in this situation; we adopted the value of $\beta = 5E$. Because of the relatively high Poisson ratio, material is forced to 'spill' out from the vertical sides below and above the bottom and top boundaries, respectively. Fairly large jumps appear near the corners to accommodate this deformation; the discontinuous approximation once more relaxes the rigid kinematic constraints imposed by the mesh. The performance of discontinuous Galerkin is in stark contrast with that of conforming piecewise linear approximations, see figure 3(b). A quick glance evinces that the conforming elements definitively encounter difficulties at the corners, and that these end up polluting the entire solution. The main evidence is that the symmetry of the problem has been broken, in no doubt caused by the particular structure of the mesh at the corners. In this case, no amount of recursive subdivision of the mesh will give a symmetric solution, the mesh must be restructured. This example suggests a clear advantage of the discontinuous Galerkin methodology; the solution is much less prone to feel the accidental kinematic constraints imposed by the mesh, as opposed to conforming methods, which in this case do not give a realistic solution.

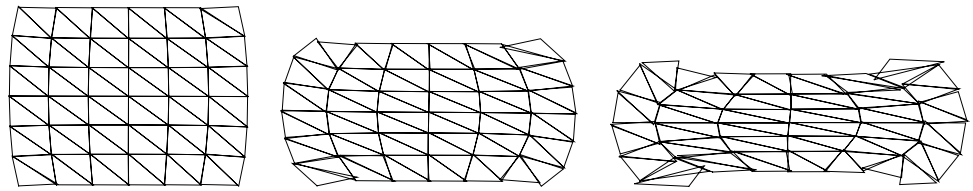

(a) Snapshots for the discontinuous Galerkin solution

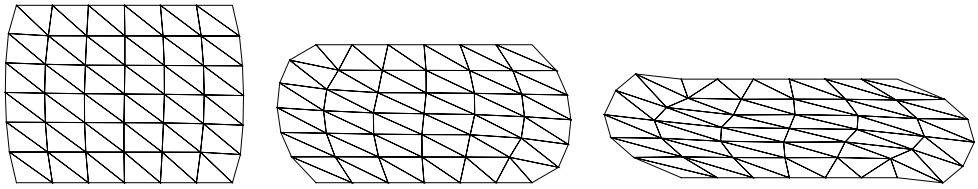

(b) Snapshots for the conforming approximation solution

Figure 3. Vertical compression of the square block. Comparison between the stabilized discontinuous Galerkin solution and the one obtained using conforming piecewise linear approximations. Because of the mesh, the symmetry of the problem is not preserved by the latter, rendering a solution that is basically very far from the exact one. Notice that a recursive subdivision of the mesh will not solve this problem, regardless of how fine the mesh becomes. This illustrates and suggests a powerful advantage of the discontinuous Galerkin approach, by substantially reducing the dependence of the solution on accidental kinematic constraints imposed by the mesh.

6.3. Stability studies

The discussion in section 4 showed that if some material and geometric conditions are met during the quasistatic evolution, the spurious appearance of buckling modes in the discrete solution can be prevented provided the stabilization parameter is large enough. In the following example we demonstrate that stabilization is very often needed, and how it affects the solutions.

The expansion example in section 6.1 shows that occasionally stabilization is not necessary, in contrast to the compressed square block example in the same section. We show next a more comprehensive study of the effect of stabilization in this last case. For this test, the square block was quasistatically loaded in 1000 steps until it reached half of its original height. At each step the position of the top surface of the block was displaced by a fixed amount. The value of the stabilization parameter was uniformly increased with the loading step, i.e., $\beta(i) = i\Delta\beta$, where i is the loading step number and $\Delta\beta \geq 0$. Three different values for $\Delta\beta$ were considered, 10^{-2} Pa/step, 10^{-3} Pa/step and 10^{-4} Pa/step. Figure 4 shows the evolution of the smallest eigenvalue of the matrix that represents the discrete second variation, equation (37), in V_h^d. Consistent with the analysis in section 4, the amount of stabilization changes with the loading, and for the compressive case, grows as the material becomes more stressed. This is reflected in that the larger the stabilization rate $\Delta\beta$, the farther the loading path can be traveled. Another important conclusion from this figure is that the discrete linearized problem may in fact be unstable with no stabilization, and in this case it is possible to stabilize it. We have yet to find a case in which the exact linearized elasticity problem is stable, but for which no value of β would help stabilize its discrete counterpart. This may occur if $k_1 > k_{1h}$.

For completeness, figure 5 shows snapshots of the deformed configuration either at the end of

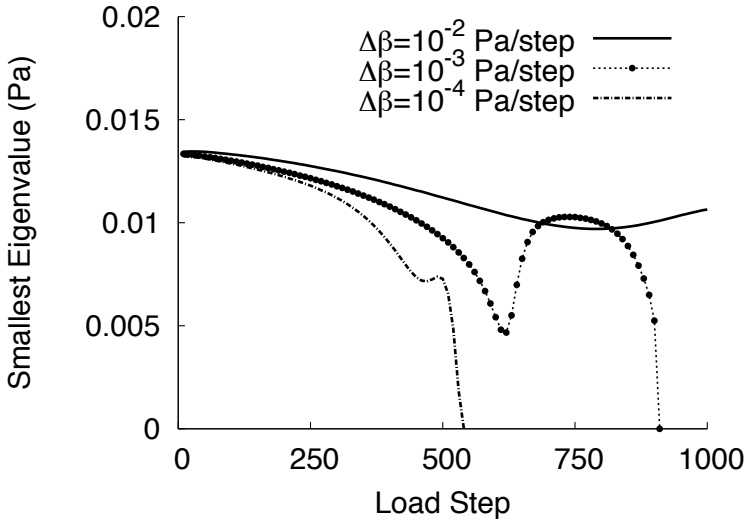

Figure 4. Evolution of the smallest eigenvalue of the matrix that represents the discrete second variation, equation (37), in V_h^d as a function of the loading step. The value of the stabilization parameter β grows by $\Delta\beta$ at each loading step, and three different values of $\Delta\beta$ are shown. While the two cases with lower $\Delta\beta$ become artificially unstable before the loading path is completed, the third case has enough stabilization to remove this pathology.

the loading path, figure 5(a), or at the onset of instability, figures 5(b) and 5(c). The instability highlights the effects of weakly enforcing Dirichlet boundary conditions, as clearly evidenced at the bottom and top surfaces of the block in figures 5(b) and 5(c); these surfaces are no longer straight.

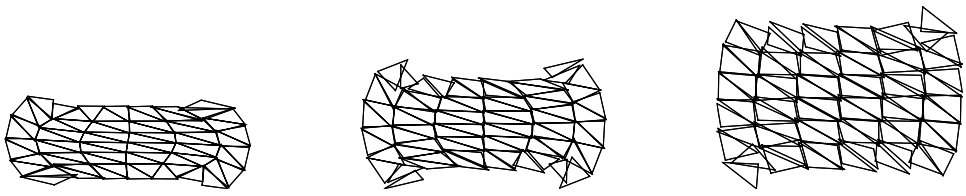

(a) $\Delta\beta = 10^{-2}$ Pa/step (b) $\Delta\beta = 10^{-3}$ Pa/step (c) $\Delta\beta = 10^{-4}$ Pa/step

Figure 5. Snapshots of the deformed configuration of the block at the end of the loading path, figure 5(a), and at the onset of instability, figures 5(b) and 5(c).

6.4. Convergence rates

As mentioned in the introduction, one of the gratifying surprises we found in evaluating the performance of the proposed discontinuous Galerkin method is that, against established conceptions, the method *is* computationally efficient when compared with a same order conforming one. A similar result has been shown in [16]. This section presents the results supporting such assertion through two qualitatively different examples.

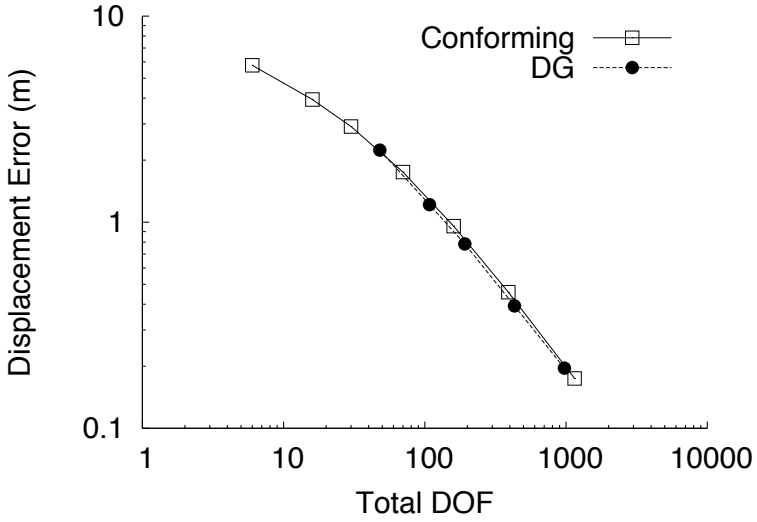

Figure 6. Plot of the L^2–norm over $\mathcal{B}_0$ of the error in the displacement field as a function of the total number of degrees of freedom for the test in section 6.1. Curves are shown for the discontinuous Galerkin method as well as for the conforming one. Remarkably, the two curves overlap, indicating that both methods provide the same accuracy for the same computational cost, i.e., for this example they are equally efficient.

We first studied the convergence of solutions for the example in section 6.1, where an elastic square block is pulled from its top surface. Only ν was changed for this test, to be $\nu = 0.45$, and again no stabilization was needed. Solutions were obtained with both the discontinuous Galerkin and the conforming method for a number of different meshes. To compute the errors, we used a very fine numerical solution calculated with 79,202 conforming linear triangles in lieu of an apparently nonexistent exact analytical solution. Figure 6 shows the L^2–norm of the error as a function of the total number of degrees of freedom. It should be noted that numerical solutions with the same number of degrees of freedom furnished by each one of the methods were necessarily computed with different meshes; the discontinuous Galerkin mesh is *coarser* than the conforming one. The use of the total number of degrees of freedom is consequently a fair measure of the computational cost involved in each calculation. It is remarkable that both curves are essentially on top of each other; both methods are equally efficient in computing these solutions.

Two observations are nevertheless pertinent. The discontinuous Galerkin method needs at least 3 gauss points in each element to integrate the piecewise linear DG–derivatives, in contrast to the single gauss point per element needed for conforming cases. There is no clean and simple

way to account for this factor within the computational cost in figure 6; however, for the neohookean material model only a small correction to the above results can be expected, with the core computational cost accounted for in the solution of the linear systems of equations. A second and to some extent obvious remark is that there are numerous instances where conforming methods have a clear advantage over discontinuous Galerkin. For example, if the exact solution is linear, no gain can be expected from allowing discontinuities to appear. A similar behavior can be anticipated when the exact solution is very smooth, since for fine enough meshes the approximated field will be nearly linear at the length scale of the mesh; we discuss more about this at the end of this section. In any event, these observations should not lessen the very desirable fact that the discontinuous Galerkin method is likely to be more computationally efficient than a conforming one when coarser meshes are used.

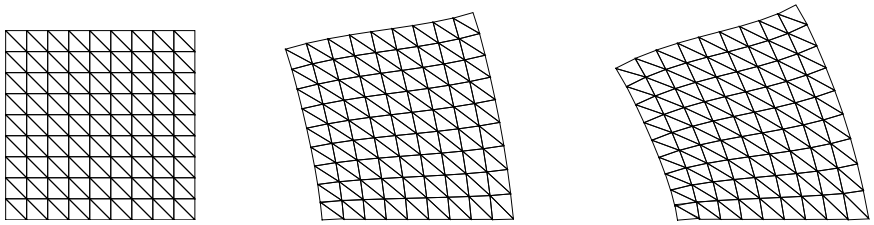

Figure 7. Snapshots of the elastic block fixed at the bottom surface and steadily loaded on its upper surface with horizontal tractions.

We now examine a deformation where the selection of the stabilization parameter strongly influences the performance of a discontinuous Galerkin solution. In this test we used the same elastic square block of section 6.1, but changed ν to be 0.15. The bottom surface of the block was held fixed and a traction of 0.02 Pa was applied parallel to the top surface. The resulting deformations have predominantly shear and bending efforts. For the first example in this section stabilization was unnecessary and no compressive stresses were present; this test however, displays strong compressive stresses, and stabilization is critical. The loading path consisted in 250 incremental loading steps in which the traction on the upper surface was uniformly varied. Snapshots of the deformed configuration during the loading path are shown in figure 7.

As in the previous example, a highly refined numerical solution with a conforming discretization served the role of the exact field for the computation of errors. The stabilization parameter was uniformly varied with the loading step. The resulting convergence plots are shown in figure 8, with curves for $\Delta\beta = 10^{-3}$ Pa/step and $\Delta\beta = 10^{-2}$ Pa/step, together with the errors for the piecewise linear conforming solutions. Notably, the discontinuous Galerkin method outperforms the conforming one for coarse meshes, provided the stabilization parameter is not too large. Naturally, when the value of β is increased, discontinuities are more strongly penalized and the discontinuous Galerkin method resembles more to a conforming one. As a consequence, a loss in efficiency for the discontinuous Galerkin method is evidenced in the choice of $\Delta\beta = 10^{-2}$ Pa/step.

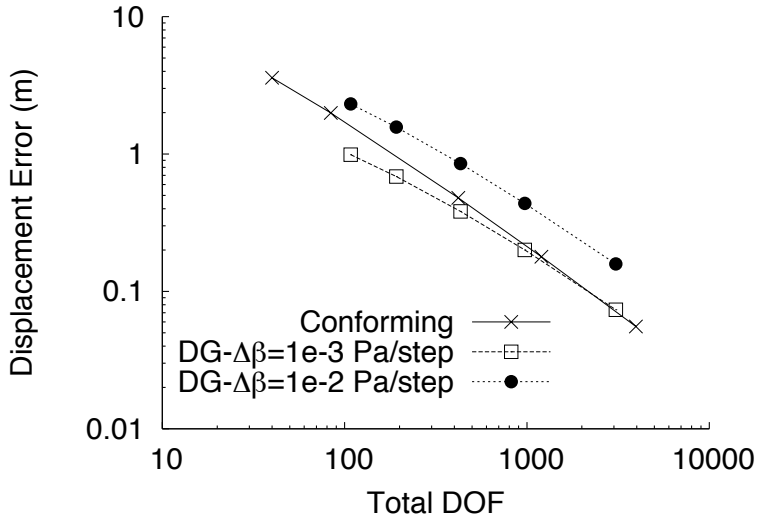

Figure 8. Plot of the L^2–norm over $\mathcal{B}_0$ of the error in the displacement field as a function of the total number of degrees of freedom used for the second example in section 6.4. In this compression and bending dominated deformations, stabilization becomes essential. An adequate choice of the stabilization parameter shows that discontinuous Galerkin is more efficient than the conforming method for rather coarse meshes. However, too much stabilization forces the discontinuous Galerkin method to resemble more to a conforming one, with an evident loss in efficiency.

Back momentarily to section 6.1, it was mentioned there that, by a direct extrapolation from the linear elastic case, the size of the jumps should asymptotically vanish when approximating smooth solutions as finer meshes are considered. This is true for the second example in this section. Figure 9 shows the L^2–norm of the lift of the jumps, $\|\mathbf{R}([\![\boldsymbol{\varphi}_h - \hat{v}(\boldsymbol{\varphi}_h)]\!])\|_{0,\mathcal{B}_0}$, as a function of the number of degrees of freedom in the mesh for two values of the stabilization parameter. Here $\boldsymbol{\varphi}_h$ is the numerical solution obtained with a mesh of characteristic element size h. Regardless of the stabilization parameter, $\|\mathbf{R}([\![\boldsymbol{\varphi}_h - \hat{v}(\boldsymbol{\varphi}_h)]\!])\|_{0,\mathcal{B}_0}$ steadily decreases with h. Moreover, note that $\|[\![\boldsymbol{\varphi}_h - \hat{v}(\boldsymbol{\varphi}_h)]\!]\|_{0,\Gamma}$ diminishes with h as well, a direct consequence of the relation $\|[\![\mathbf{v}_h]\!]\|_{0,\Gamma} \leq C^+ h^{1/2} \mathbf{R}([\![\mathbf{v}_h]\!])$ for any $\mathbf{v}_h \in V_h^d$ in equation (34), despite the fact that the number of faces in Γ, and its total area, grows as h wanes. Notice that the presence of the numerical flux inside the jump operator implies that the Dirichlet boundary conditions, weakly imposed here, become better satisfied for finer discretizations. In summary, the discontinuous Galerkin method is converging toward the smooth solution; however, at some level of mesh refinement any computational advantage for discontinuous Galerkin over a conforming method usually subsides.

6.5. A note about stresses

The stresses generated at the final configuration of the second example in section 6.4 are depicted in Figure 10. Shown there is a contour plot for the P_{XX} component of the first Piola–Kirchhoff stress tensor, where X is the horizontal direction to the right in the picture. The stress components were computed by using the equivalent three–field variational principle,

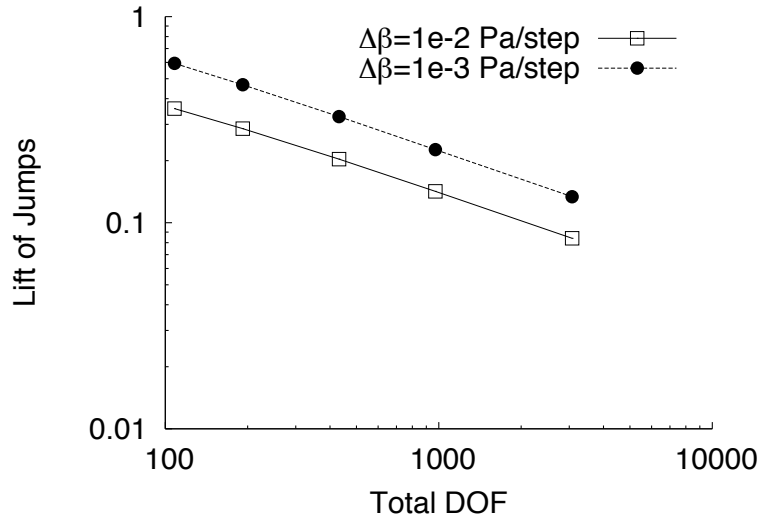

Figure 9. Evolution of $\|\mathbf{R}([\![\boldsymbol{\varphi}_h - \hat{v}(\boldsymbol{\varphi}_h)]\!])\|_{0,\mathcal{B}_0}$, a measure of the size of discontinuities, as a function of the number of degrees of freedom in the solution $\boldsymbol{\varphi}_h$ for the second example in section 6.4. Like in the linear elastic case, the discontinuities in the discrete approximations asymptotically vanish as the mesh if refined, regardless of the value of the stabilization parameter.

equation (26). It was seen in [22] that in the stress–free linear elastic case the hitherto defined stresses converge. The resulting stress field is rather smooth; this, however, was not occasionally the case for some other examples. Even though for this nonlinear case stresses may eventually converge in L^2–sense as well, a better method to compute them might be worth exploring.

6.6. Incompressible limit

We proceed next to explore the properties of the current discretization on near incompressible situations. For the stress–free linear elastic case several authors [40, 16] have proposed low–order discontinuous Galerkin methods that do not lock in near incompressible situations. When compared to mixed formulations, discontinuous Galerkin methods in their primal formulation [16] possess the clear advantage of being computationally efficient and not needing to carry the additional pressure field.

In the nonlinear elasticity large deformation regime, however, the situation is more dire, but some of the same ideas from the linear case still apply. The fundamental difference with the linear elastic case is that the constraint is now nonlinear. More precisely, $\det \mathbf{F} = 1$ everywhere in the body, instead of a divergence free condition. The most elegant solution is perhaps the use of mixed formulations, see, e.g., [36], but selective reduced integration, with its associated loss in accuracy, is also an often used alternative. We show here that numerical results suggest that the proposed discontinuous Galerkin method using low–order elements does not lock in near incompressible situations for the nonlinear elasticity, large deformation regime.

The numerical example to consider consists of a thick–walled cylindrical tube with imposed displacements at the inner wall and stress–free at the outer wall, with no axial strain. This example benefits from having an exact analytical solution, see e.g., [15], which follows

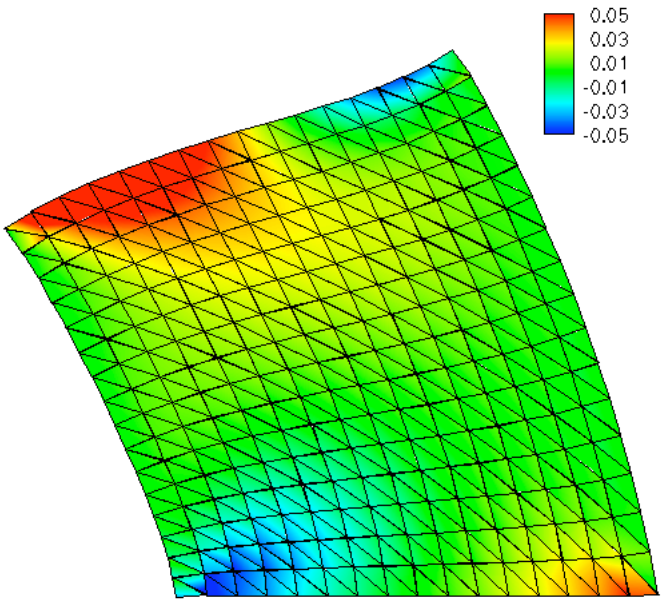

Figure 10. Contour plot depicting the P_{XX} component of the first Piola–Kirchhoff stress, where X is the horizontal direction to the right, for the final configuration of the second example in section 6.4. Stresses were computed through the equivalent three–field variational principle, equation (26).

easily from requiring the deformation mapping to be axysymmetric and to satisfy the incompressibility constraint. The analytical solution is

$$r(R) = \sqrt{r_0^2 + R^2 - R_0^2}, \tag{78}$$

where $r(R)$ is the radius of a deformed circle originally of radius R in the undeformed tube, and r_0 and R_0 are the deformed and original inner radius of the tube, respectively. For a neohookean material the first Piola–Kirchhoff stress is

$$\mathbf{P} = \lambda \log(\det \mathbf{F}) \mathbf{F}^{-\mathsf{T}} + \mu \left(\mathbf{F} - \mathbf{F}^{-\mathsf{T}} \right), \tag{79}$$

which in the incompressible limit has $\lambda \to \infty$ with fixed E and hence $\lambda \log(\det \mathbf{F}) \to p$, the value of a partial pressure, defined up to a free additive constant that is determined solely by the boundary conditions. The exact distribution of the normal component of the traction per unit undeformed area on a cylindrical surface of undeformed radius R is given by

$$T_R(R) = \mathbf{e}_R^{\mathsf{T}} \cdot \mathbf{P} \cdot \mathbf{e}_R = p \frac{r}{R} + \mu \left(\frac{R}{r} - \frac{r}{R} \right), \tag{80}$$

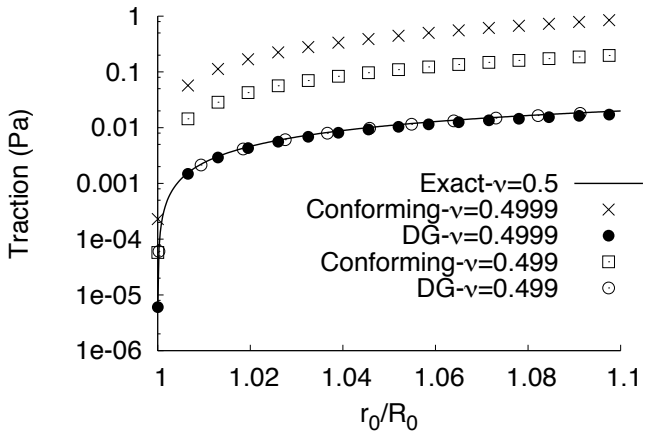

Figure 11. Evolution of the traction at the inner wall of the tube as a function of the relative expansion of the inner radius. Results computed with conforming and discontinuous Galerkin methods are shown, for two near incompressible cases, $\nu = 0.499, 0.4999$. The exact solution is also shown for comparison. It is apparent from these results that the discontinuous Galerkin method is locking–free.

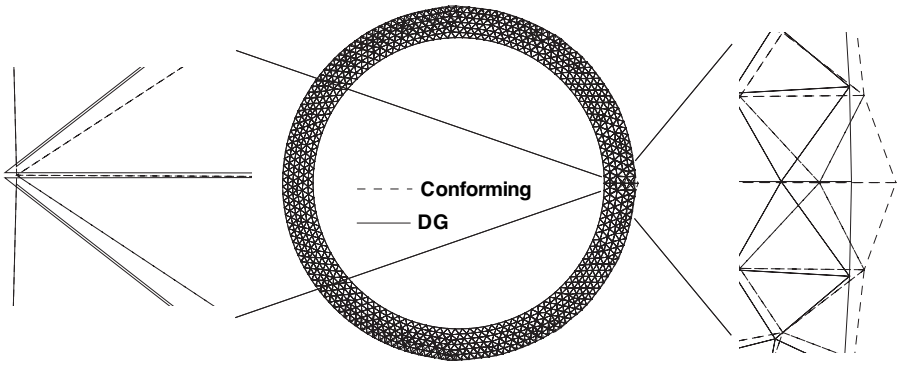

Figure 12. Comparison of the deformed configuration of the tube computed with the two methods at the final configuration, after 20,000 loading steps. Locking in the conforming case is evidenced by the highlighted bump on the outer wall shown in the augmented view on the right, a consequence of high stresses and the kinematic constraints of the mesh. In contrast, a smooth outer wall is predicted by the discontinuous Galerkin method. The enlarged image on the left shows the presence of jumps in the discontinuous Galerkin solution to accommodate the incompressibility constraint.

where $\mathbf{e}_R$ is a unit vector in the radial direction from the axis of the cylinder. For a cylinder with an undeformed outer radius $R_1 > R_0$, the condition $T_R(R_1) = 0$ and the equilibrium equations determine the value of $p(R)$, given by

$$p(R) = \mu \left[\frac{(r_0^2 - R_0^2)}{r_1^2} \left(\frac{R_1^2 - R^2}{2r^2} + 1 \right) - \log \left(\frac{r/R}{r_1/R_1} \right) \right], \tag{81}$$

where $r_1 = r(R_1)$. In the current example $R_0 = 1$ m and $R_1 = 1.25$ m, while $E = 1$ Pa.

Locking examples generally consist of a discretized body loaded with some force distribution. As the incompressibility limit is approached the deformation induced by the force distribution tends asymptotically to zero, it "locks", while the exact solution does show a deformed body in the same limit. In contrast, we impose the displacements at the inner wall of the cylinder, and consequently locking of the numerical solution is manifested with the magnitude of the forces imposed on the inner wall to attain the prescribed displacement diverging to infinity as the incompressibility limit is approached. The precise quantity we monitor is the radial component of the traction per unit *deformed* area at the inner wall, to wit

$$t_{\text{inner}} = \mathbf{e}_R^{\mathsf{T}} \cdot \boldsymbol{\sigma}(R_0) \cdot \mathbf{e}_R = T_R(R_0) \frac{R_0}{r_0}.$$

The cross–section orthogonal to the axis of the hollow cylinder was discretized with 1677 linear triangles, and solutions with $\nu = 0.499$ and $\nu = 0.4999$ for both discontinuous Galerkin and conforming methods were obtained. Of course, the latter is known to lock under these conditions, so it only serves for the purpose of comparison. The quasistatic loading path consisted on varying the inner radius of the tube by a fixed amount at each loading step. A total of 20,000 loading steps were used to get to a maximum inner radius $r_1 = 1.1R_1$; the large value of λ makes it difficult to take large loading steps. As in section 6.3, the stabilization parameter β was uniformly varied with the loading step, with $\Delta\beta = 10^{-4}$ Pa/step.

The results for these tests are shown in figure 11, where the computed evolutions for t_{inner} as a function of r_0/R_0 are plotted together with the exact one, for up to 10% inner radial expansion. As expected, the value of t_{inner} returned by the conforming approximation worsens as the material becomes more incompressible. In contrast, discontinuous Galerkin solutions remain close to the exact one for the two values of ν; this demonstrates that the discontinuous Galerkin approximation is pretty insensitive to the specific value of $\nu \approx 0.5$. A comparison of the deformed configurations of the tube for the two methods is shown in figure 12, with $\nu = 0.4999$. The locking of the conforming solution is manifested through the formation of a small bump on the outer wall of the tube; the discontinuous Galerkin solution predicts a smooth outer wall. A more insightful perspective is obtained from the plot of the error in t_{inner} as a function of r_0/R_0, in figure 13, showing only the discontinuous Galerkin solutions with $\nu = 0.499$ and $\nu = 0.4999$ with $\Delta\beta = 10^{-4}$ Pa/step, and $\nu = 0.4999$ with $\Delta\beta = 10^{-5}$ Pa/step. In a comparison between the first two cases, the most noticeable feature is that the error in the solution increases slightly as the material becomes more incompressible, albeit at a substantially slow rate when compared to the conforming approximation. Fears that the discontinuous Galerkin method may eventually lock as ν gets closer to 0.5 are somewhat placated by the comparison between the second and third cases, which have essentially the same error for the two different values of ν, at the cost of reducing the value of the stabilization parameter. These results strongly suggest the absence of locking for the discontinuous Galerkin method in the *large* deformation regime. From a practical perspective, the performance of the discontinuous Galerkin method with low–order elements is *effectively* free of locking.

6.7. Three–dimensional examples

Thus far, all simulations presented have been restricted to two dimensional examples, for their lower computational cost makes them more convenient to study the numerical properties of the method. We now illustrate the behavior of the method through a couple of three–dimensional examples.

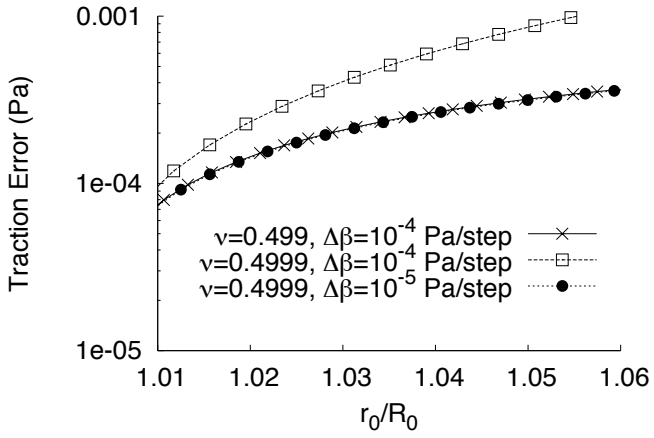

Figure 13. Error in the computed traction on the inner wall of the deformed tube as a function of the relative change of the inner radius, r_0/R_0, for three different cases. Notice that the error grows very slowly when ν gets closer to 1/2 with constant $\Delta\beta$, at a much lower pace than the error for the conforming solutions; compare with figure 11. In fact, by relaxing the value of the stabilization parameter virtually the same error is obtained for the two values of ν. This demonstrates that from a practical perspective, discontinuous Galerkin is effectively locking free in the large deformations regime.

The first case consists of a deforming cylinder under compression. The cylinder is made of the neohookean material extended to the compressible range in equation (51), with $E = 30$ GPa and $\nu = 0.45$. In this test the stabilization parameter β has been held constant for each loading increment and equal to 100 GPa. The diameter and height of the cylinder are 1m and 2m, respectively, and it has been discretized into 191 linear tetrahedra. The cylinder is deformed such that its bottom face is held fixed, while the top face is translated both vertically and horizontally at a uniform rate per loading step, up to a maximum of 1m and 0.14m, respectively. The resulting deformations in the cylinder can be roughly described as predominantly compressive with some shear, as revealed in the snapshots in figure 14 showing the deformed configuration of the cylinder throughout the loading path. Notice that once the cylinder has reached the halfway point of the loading path, the solution displays strong discontinuities, as well as an emerging localization of the deformation, a possible sign for buckling. This demonstrates the method is capable of predicting configurations with very large deformations.

The purpose of the second example is to demonstrate the use of the method in more complex three–dimensional geometries with a wide range of material properties and boundary conditions. Inspired by the surgical procedure of stent angioplasty, we have chosen an example that is representative of a stent expanding inside a diseased artery. Figure 15 shows an idealized version of a section of the actual geometry. The inner dark section represents a stent, the light section represents the atherosclerotic plaque, and the outer dark section represents the blood vessel wall. For the illustrative purposes in this paper and to show the feasibility of using discontinuous Galerkin to model the expansion of the stent, it is enough to consider very simple material models for the three regions; in this case all regions have been assumed to

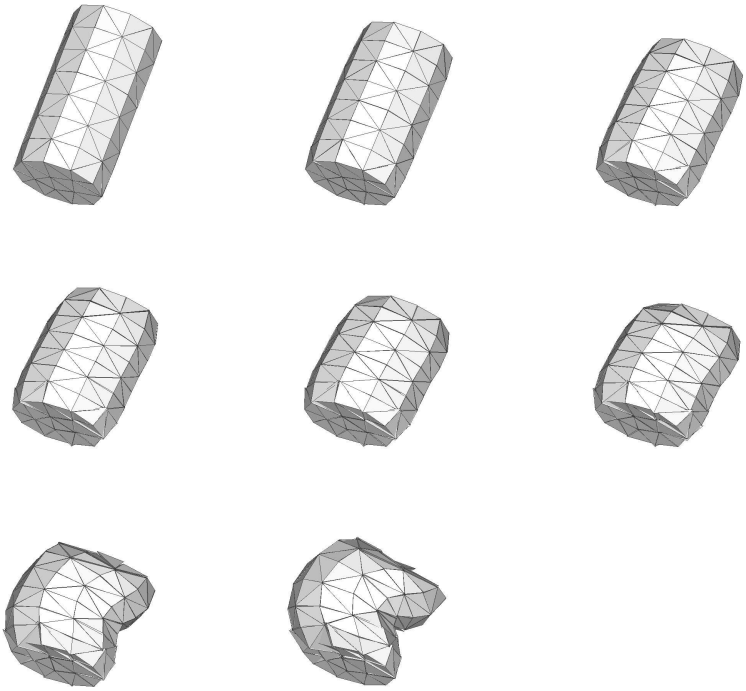

Figure 14. Sequence of snapshots for the compressed cylinder.

have the neohookean behavior given in equation (51). Of course, any predictive model for this situation has to necessarily include more complex constitutive behaviors, such as the anisotropy induced in the arterial wall by collagen fibers, see e.g., [17]. Similarly, the dimensions of the stent have been assumed to be much larger than the real ones, only for simplicity. All relevant dimensions and material properties for this example are given in table I. One of the interesting features of this example is the use of radically different material properties for each region.

Section	Inner Radius	Outer Radius (cm)	ν	E (Pa)
Stent	0.40	0.50	0.33	10^5
Plaque	0.50	0.75	0.25	10^{-2}
Wall	0.75	0.90	0.46	10^2

Table I. Geometric and material properties of the idealized stent angioplasty model

Only one–third of the stent has been simulated, and for simplicity traction free boundary conditions have been used on the two resulting lateral sections. Figure 16(a) shows the mesh in the undeformed configuration. Notice that the plaque occupies a large section of the artery, but not its entire length. Compressive tractions have been imposed along the radial direction in both the radially innermost surface of the stent and the outer cylindrical surface of the artery, equal to 1 Pa and 10^{-3} Pa, respectively. Rigid body displacements have been prevented by

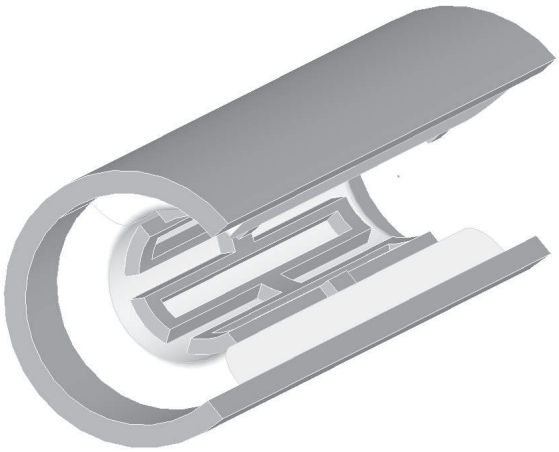

Figure 15. Idealized geometric arrangement of a diseased artery and contracted stent. The vessel and plaque are cylinders, but a pie–shaped part has been removed for the illustration. The outer gray cylinder represents the artery, the inner white cylinder the plaque, on top of which lies the stent, also in gray.

holding the outermost edges on the cross–sections orthogonal to the axial direction fixed. The stabilization parameter was uniformly increased by $\Delta\beta = 10^4$ Pa/step, through a total of 360 loading steps that steadily augmented the imposed tractions to their stated value. No efforts have been made to optimize $\Delta\beta$ for this example.

The resulting deformed configuration is shown in figure 16(b), while figure 17 shows the evolution of radial displacements during the loading path through a sequence of contour plots. At the final configuration the inner radius of the stent has increased over 40%, and it has been completely absorbed into the soft plaque. In this example, highly compressive deformations are present and are gracefully handled by the proposed stabilized method.

7. SUMMARY AND CONCLUSIONS

We proposed a framework to generate very efficient discontinuous Galerkin methods for nonlinear elasticity, based on the utilization of the lifting operators and the DG–derivative. The resulting methods are singled out by the particular choice of finite element spaces and numerical fluxes. Regardless, all methods have a variational structure and can be equivalently formulated into three–field variational principles involving stresses, strains and displacements as independent variables. As often done for linear problems, some form of stabilization is needed, and a standard one was considered for the specific choice of Bassi and Rebay numerical fluxes. In this context, we discussed the concept of linearized stability, and proposed a sufficient

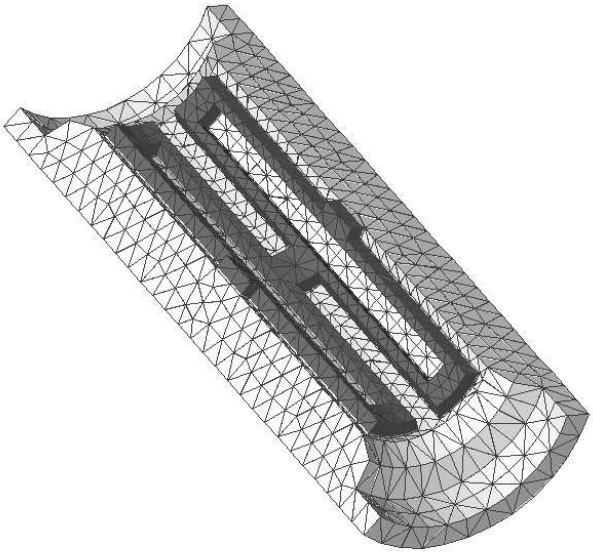

(a) Undeformed stent and artery

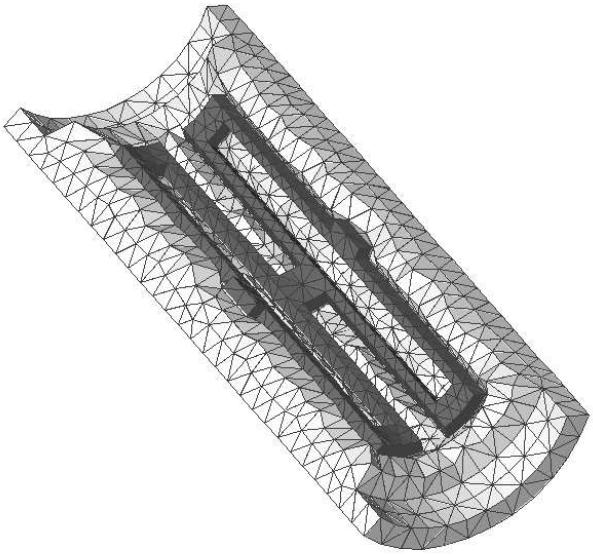

(b) Deformed stent and artery

Figure 16. Idealized stent angioplasty simulations with discontinuous Galerkin

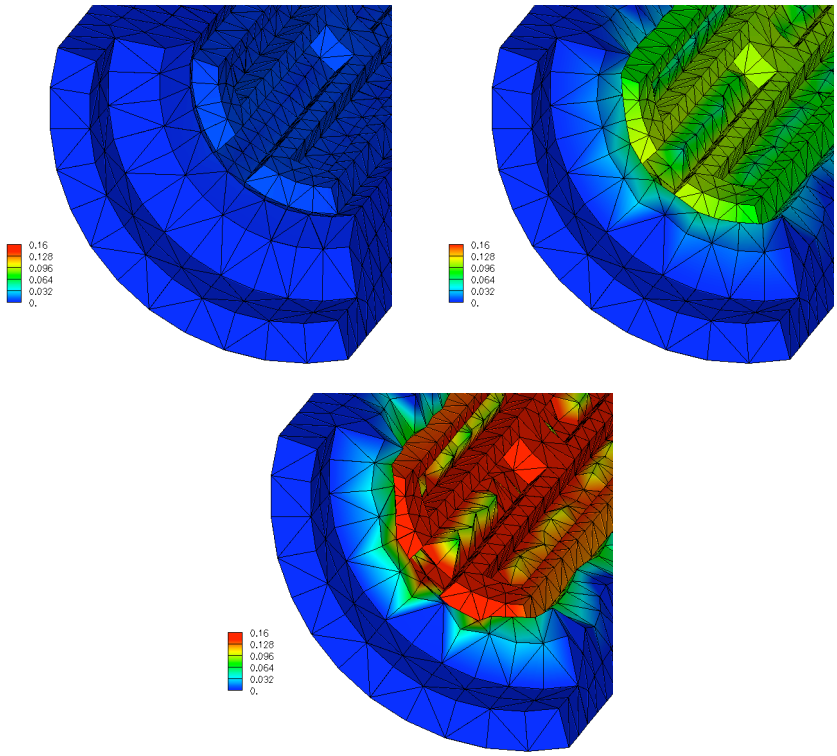

Figure 17. Sequence of snapshots during the loading of the stent from the undeformed configuration. The contour plots show the magnitude of the radial displacements.

condition that involves both material and geometric parameters. We proved then that if this condition is satisfied, the discontinuous Galerkin method provides linearly stable configurations as long as the stabilization parameter is large enough; a lower bound for the latter was computed. We then discussed some general features of the implementation of these methods, attempting to dismiss their apparent complexity. By pre–computing a number of quantities, such as the lifting operator and the stabilization term, only a loop over the elements in the mesh needs to be performed at each iteration for the nonlinear solver; no loop over the element faces is needed. We demonstrated the performance of the method with the Bassi and Rebay numerical fluxes through a number of numerical examples. We found that jumps in fact appeared in the discrete solution even when the exact one was smooth, and that these gradually waned as finer meshes were considered. Stabilization may occasionally not be needed, but it plays an important role whenever compressive stresses are present, at least for the neohookean material model used in these examples. The discontinuous Galerkin method has been found to outperform conforming approximations in the presence of some mesh–based kinematic constraints, elegantly sidestepping the latter through discontinuities between elements. We showed the very often the discontinuous Galerkin method is more efficient than a conforming one, with this relative advantage vanishing as the stabilization parameter grows or

the meshes become too fine. When confronted with near incompressible situations, numerical examples suggest that the discontinuous Galerkin method with piecewise linear elements is free of locking in the large deformation regime, with no need of a separately interpolated pressure field characteristic of mixed methods. Finally, we demonstrated the performance of the method for two three–dimensional examples.

An important yet unresolved problem that emerges from this work is the automatic and efficient selection of the stabilization parameter. This has crippled past attempts to make discontinuous Galerkin methods competitive, but it is worth taking a fresh look. For these examples the choice of β was never a substantial problem, since we have generally adopted values in the same order of the prevailing stresses.

Likewise, the computation of stresses through L^2 projections as in equation (26) often provides non–smooth stress fields, even though in the linear elastic case, for example, stresses have been proved to converge in L^2–sense. Perhaps a smoother approximation can be constructed.

ACKNOWLEDGEMENTS

We thank Deborah Sulsky and Patrizio Neff for helpful discussions during the creation of this manuscript. This work was funded by the National Institutes of Health through the NIH Roadmap for Medical Research, Grant U54 GM072970. Information on the National Centers for Biomedical Computing can be obtained from `<http://nihroadmap.nih.gov/bioinformatics>`.

REFERENCES

1. D. N. Arnold. An interior penalty finite element method with discontinuous element. *SIAM J. Numer. Anal.*, 19:742–760, 1982.
2. Douglas N. Arnold, Franco Brezzi, Bernardo Cockburn, and L. Donatella Marini. Unified analysis of discontinuous galerkin methods for elliptic problems. *SIAM J. Numer. Anal.*, 39(5):1749–1779, 2002.
3. Ivo Babuska and Milos Zlamal. Nonconforming elements in the finite element method with penalty. *SIAM J. Numer. Anal.*, 10(5):863–875, 1973.
4. J.M. Ball. Some open problems in elasticity. In *Geometry, Mechanics and Dynamics*. Springer, 2002.
5. F. Bassi and S. Rebay. High-order accurate discontinuous finite element method for the numerical solution of the compressible navier-stokes equations. *J. Comput. Phys.*, 131:267–279, 1997.
6. S. Blemker, P. Pinsky, and S. Delp. A 3d model of muscle reveals the causes of nonuniform strains in the biceps brancii. *Journal of Biomechanics*, 38:657–665, 2005.
7. S. Brenner. Korn's inequalities for piecewise H^1 vector fields. *Mathematics of Computation*, 2003.
8. S. C. Brenner and L. Scott Ridgeway. *The Mathematical Theory of Finite Element Methods*. Springer, 1994.
9. F. Brezzi, G. Manzini, D. Marini, P. Pietra, and A. Russo. Discontinuous galerkin approximations for elliptic problems. *Numerical Methods for Partial Differential Equations*, 16:365–378, 2000.
10. C. Carstensen. Ten remarks on nonconvex minimisation for phase transition simulations. *Computer Methods in Applied Mechancis and Engineering*, 194:169–193, 2005.
11. K.J. Caspersen, A. Lew, M. Ortiz, and A.E. Carter. Importance of shear in the bcc–to–hcp transformation in iron. *Physical Review Letters*, 93:115501, 2004.
12. G. Engel, K. Garikipati, T.J.R. Hughes, M.G. Larson, L. Mazzei, and R.L. Taylor. Continuous/discontinuous finite element approximations of fourth-order elliptic problems in structural and continuum mechanics with applications to thin beams and plates, strain gradient elasticity. *Computer Methods in Applied Mechanics and Engineering*, 191:3669–3750, 2002.
13. C. Farhat, I. Harari, and L.P. Franca. The discontinuous enrichment method. *Computer Methods in Applied Mechanics and Engineering*, 190:6455–6479, 2001.

14. G. Gatica, L.F. Gatica, and E.P. Stephan. A dual–mixed finite element method for nonlinear incompressible elasticity with mixed boundary conditions. Preprint 05–06, Departamento de Ingenieria Matematica, Universidad de Concepcion, 2005.
15. A.E. Green and W. Zerna. *Theoretical Elasticity*. Oxford Universtiy Press, 1968.
16. Peter Hansbo and Matt G. Larson. Discontinuous galerking and the crouzeix-raviart element: Application to elasticity. *Mathematical Modelling and Numerical Analysis*, 37(1):63–72, 2003.
17. G.A. Holzapfel. Biomechanics of soft tissue. Technical report, Institute for Structural Analysis. Graz University of Technology, 2000.
18. T.Y. Hou and X. Wu. A multiscale finite element method for elliptic problems in composite materials and porous media. *Journal of Computational Physics*, 134:169–189, 1997.
19. J. Douglas Jr. and T. Dupont. *Interior penalty procedures for elliptic and parabolic Galerkin method*, volume 58 of *Lecture Notes in Physics*. Springer-Verlag, Berlin, 1976.
20. P. Kloucek, B. Li, and M. Luskin. Analysis of a class of nonconforming finite elements for crystalline microstructure. *Mathematics of Computation*, 65(215):1111–1135, 1996.
21. A. Lew, J.E. Marsden, M. Ortiz, and M. West. Variational time integrators. *International Journal for Numerical Methods in Engineering*, 60:153–212, 2004.
22. A. Lew, P. Neff, D. Sulsky, and M. Ortiz. Optimal BV estimates for a discontinuous Galerkin method in linear elasticity. *Applied Mathematics Research Express*, 3:73–106, 2004.
23. J. E. Marsden and T. J. R. Hughes. *Mathematical Foundations of Elasticity*. Dover, Mineola, N.Y., 1994.
24. G. Dal Maso, G. Francfort, and R. Toader. Quasistatic crack growth in finite elasticity. Preprint, 2005.
25. P. Neff. On korn's first inequality with non–constant coefficients. *Proceedings of the Royal Society of Edinburgh*, 132A:221–243, 2002.
26. J. Nitsche. Über ein variationsprinzip zur löung von dirichlet problemen bei verwendung von teilräumen, die keinen randbedingungen unterworfen sind. In *Abh. Math. Sem.*, volume 36, pages 9–15, Univ. Hamburg, 1971.
27. P. Percell and M. F. Wheeler. A local residual finite element procedure for elliptic equations. *SIAM J. Numer. Anal.*, 15:705–714, 1978.
28. P. Pinsky, D. van der Heide, and D. Chernyak. Computational modeling of mechanical anisotropy in the cornea and sclera. *Journal of Cataract and Refractive Surgery*, 31(1):136–145, 2005.
29. M. Pitteri and G. Zanzotto. *Continuum models for phase transitions and twinning in crystals*. Chapman & Hall/CRC, 2003.
30. B. Rivière and M. F. Wheeler. Optimal error estimates for discontinuous Galerkin methods applied to linear elasticity problems. Technical Report 00-30, Texas Institute for Computational and Applied Mathematics, 2000.
31. J. E. Roberts and J.-M. Thomas. Mixed and hybrid methods. In Ciarlet P. .G. and J. L. Lions, editors, *Handbook of Numerical Analysis*, volume II. Elsevier Science Publishers B.V. (North-Holland), 1991.
32. G. Romano, F. Marotti de Sciarra, and M. Diaco. Well–posedness and numerical performances of the strain gap method. *International Journal for Numerical Methods in Engineering*, 51:103–126, 2001.
33. J.C. Simo and F. Armero. Geometrically non–linear enhanced strain mixed methods and the method of incompatible modes. *Computer Methods in Applied Mechanics and Engineering*, 33:1413–1449, 1992.
34. J.C. Simo and T.J.R. Hughes. On the variational foundations of assumed strain methods. *Transactions of the ASME Journal of Applied Mechanics*, 53:51–54, 1986.
35. J.C. Simo and T.J.R. Hughes. *Computational Inelasticity*. Springer, 1997.
36. P. Le Tallec. Incompressibility in finite elements. In L.P. Franca, T.E. Tezduyar, and A. Masud, editors, *Finite Element Methods: 1970's and Beyond*, pages 33–45. CIMNE, Barcelona, 2004.
37. P. Thoutireddy and M. Ortiz. A variational r–adaption and shape–optimization method for finite–deformation elasticity. *International Journal for Numerical Methods in Engineering*, 61:1–21, 2004.
38. L.R.G. Treloar. *The physics of rubber elasticity*. Oxford: Clarendon Press, 1975.
39. M. F. Wheeler. An elliptic collocation-finite element method with interior penalties. *SIAM J. Numer. Anal.*, 15:152–161, 1978.
40. T.P. Wihler. Locking–free dgfem for elasticity problems in polygons. *IMA Journal of Numerical Analysis*, 24:45–75, 2004.